Journal of Geophysical Research: Oceans

RESEARCH ARTICLE
10.1029/2017JC013625

Tidal Flow Asymmetry Owing to Inertia and Waves on an Unstratified, Shallow Ebb Shoal

Anna Wargula[1], Britt Raubenheimer[2], Steve Elgar[2], Jia-Lin Chen[3], Fengyan Shi[4], and Peter Traykovski[2]

[1]United States Naval Academy, Annapolis, MD, USA, [2]Woods Hole Oceanographic Institution, Woods Hole, MA, USA, [3]National Cheng Kung University, Tainan City, Taiwan, [4]University of Delaware, Newark, DE, USA

Key Points:
- Flow inertia and ebb channelization result in tidal flow asymmetry on an ebb shoal
- Waves drive local and nonlocal changes to water levels in and near the inlet
- Wave-driven changes to flows and water levels affect the tidal flow asymmetry

Correspondence to:
A. Wargula,
wargula@usna.edu

Citation:
Wargula, A., Raubenheimer, B., Elgar, S., Chen, J.-L., Shi, F., & Traykovski, P. (2018). Tidal flow asymmetry owing to inertia and waves on an unstratified, shallow ebb shoal. *Journal of Geophysical Research: Oceans*, *123*. https://doi.org/10.1029/2017JC013625

Received 13 NOV 2017
Accepted 24 JUL 2018
Accepted article online 6 AUG 2018

Abstract Observations of water levels, waves, currents, and bathymetry collected for a month at an unstratified tidal inlet with a shallow (1 to 2 m deep) ebb shoal are used to evaluate the asymmetry in flows and dynamics owing to inertia and waves. Along-channel currents ranged from −1.5 to 0.6 m/s (positive inland) inside the main (3 to 5 m deep) channel crossing the ebb shoal. Net discharge is negligible, and ebb dominance of the channel flows is owing to inflow and outflow asymmetries near the inlet mouth. Offshore wave heights ranged from 0.5 to 2.5 m. During moderate to large wave events (offshore significant wave heights >1.2 m), wave forcing enhanced onshore mass flux near the shoal edge and inside the inlet, leading to reduced ebb flow dominance. Momentum balances estimated with the water depths, currents, and waves simulated with a quasi 3-D numerical model reproduce the momentum balances estimated from the observations reasonably well. Both observations and simulations suggest that ebb-dominant bottom stresses are balanced by the ebb-dominant pressure gradient and the tidally asymmetric inertia, which is a sink (source) of momentum on flood (ebb). Simulations with and without waves suggest that waves drive local and nonlocal changes in the water levels and flows. Specifically, breaking waves at the offshore edge of the ebb shoal induce setup and partially block the ebb jet (local effects), which leads to a more onshore-directed mass flux, changes to the advection across the ebb shoal, and increased water levels inside the inlet mouth (nonlocal effects).

Plain Language Summary Inflow (flood) and outflow (ebb) from coastal river inlets drive the exchange of nutrients, pollutants, and biota between inland waters and the ocean. Measurements and computer models of flows, water levels, and waves at New River Inlet, NC, were used to understand how tides and waves affect flood and ebb flow patterns. New River Inlet has a shallow *ebb shoal*, a pile of sand that extends from the mouth to nearly 1 km offshore. Flood flows over the shoal are shown to funnel into the inlet radially from all sides of the inlet mouth, whereas ebb flows leave the inlet in a concentrated jet. Owing to this asymmetry in flood versus ebb, tidally averaged flows on the ebb shoal were seaward directed. Breaking waves at the offshore edge of the ebb shoal changed the flows and water levels across the entire ebb shoal. The water level is elevated and flows toward the inlet are enhanced where breaking wave momentum fluxes were large (local effects). The enhanced flow toward the inlet mouth elevated water levels inside the inlet where wave breaking was minimal (nonlocal effects).

1. Introduction

Asymmetries in flows and dynamics in and near tidal inlets affect the exchange of water masses, nutrients, sediments, and biota between inland waters and the coastal ocean. Flow asymmetries in tidal inlets can arise from many sources, including river discharge or mass exchange with connected inlets (Boon & Byrne, 1981; Pacheco et al., 2010; Salles et al., 2005), tidal distortion and the generation of overtides in shallow water (Blanton et al., 2002; Friedrichs & Aubrey, 1988, 1994; Speer & Aubrey, 1985), Stokes drift (Li & O'Donnell, 1997), geometric effects leading to tidal differences in horizontal flow structure (Hench & Luettich, 2003; Stommel & Farmer, 1952), and bathymetric-induced flow variations over channels and shoals (Buijsman & Ridderinkhof, 2007; Hench & Luettich, 2003; Li & O'Donnell, 1997, 2005). Although these processes often result in tidal asymmetries in the flow inertia and frictional dissipation (Friedrichs & Aubrey, 1988; Hench et al., 2002), there are few field studies that resolve the relative importance of these two terms (Geyer et al., 2000). In addition, although many studies have evaluated the momentum balances at inlets (Blanton et al., 2002; Buijsman & Ridderinkhof, 2007; Geyer et al., 2000; Hench et al., 2002; Hench & Luettich, 2003), the contribution of waves is not understood well.

Numerical simulations suggest that wave forcing affects water fluxes and momentum in ocean inlets (Bertin et al., 2009; Chen et al., 2015; Dodet et al., 2013; Gong et al., 2018; Malhadas et al., 2009; Olabarrieta et al., 2011; Piedracoba et al., 2005). Wave heights and wave breaking are tidally modulated at inlets owing to changing flows and water depths (Kang & Di Iorio, 2006), leading to spatially and temporally varying wave effects on the flows and dynamics (Bertin & Olabarrieta, 2016). Model simulations and field observations suggest wave momentum flux (radiation stress) gradients owing to dissipation across the ebb shoal can decrease the offshore extent of the ebb jet (Olabarrieta et al., 2014) and drive fluxes into the inlet (Bertin et al., 2009; Chen et al., 2015; Gong et al., 2018; Malhadas et al., 2009; Orescanin et al., 2014; Wargula et al., 2014), resulting in increased bay water levels (Dodet et al., 2013; Olabarrieta et al., 2011). Along the shoreline on either side of the inlet, cross-shore decreases in wave radiation stresses owing to wave breaking are balanced by increases in the mean sea level (setup; Apotsos et al., 2007, 2008; Longuet-Higgins & Stewart, 1964; Raubenheimer et al., 2001), which may enhance flows converging on the inlet (Bertin et al., 2009). If an inlet connected to an enclosed bay has asymmetric shoals, wave-driven flows on one side of the inlet may be balanced by a return flow on the opposite side, leading to a cross-inlet variable response to waves (Piedracoba et al., 2005). In addition, depending on the jet outflow rate, wave energy, and inlet morphology, wave-forced flows may constrict the ebb current jet, causing it to narrow and intensify in the main inlet channel (Chen et al., 2015; Olabarrieta et al., 2011, 2014) or force currents alongshore of the ebb shoal (Feddersen et al., 2016).

Here in situ field measurements (section 3) and quasi 3-D numerical model simulations (section 4, evaluated in section 5) of water levels, currents, and waves at an unstratified tidal inlet with complex bathymetry are used to show the importance of flow inertia (advection) and waves to tidal flow asymmetry (section 6). The observations and simulations also are used to investigate how waves drive setup and affect flows on a shallow ebb shoal (section 6).

2. Site Location

New River Inlet, located ~100 km south of Cape Hatteras, North Carolina, is 1,000 m wide at the mouth and tapers to 200 m wide about 800 m inland where there is a 90° bend (Figure 1). The shallow ~800-m radius semicircular ebb shoal is 1 to 2 m deep (Figure 1, red-yellow contours). There are two channels extending across the ebb shoal, including one that was dredged in April 2012 (3 to 5 m deep, to the southwest) and one that is a remnant of a former main channel (2 m deep, to the northeast).

The bathymetry was surveyed (relative to NAVD88, which corresponds roughly to mean sea level) five times (16–17 April and 1–2, 10–11, 17–18, and 25 May) in 2012. Temporal changes in the sand levels on the ebb shoal and in the inlet mouth typically were less than 0.3 m, and the momentum balance results are not sensitive to which bathymetry is used (elevation changes at the sensors used in the momentum balance analysis were less than 0.1 m). Thus, bathymetry from 10 to 11 May, the middle of the study period, is used here.

New River extends about 25 km upstream from the inlet, and the backbay (Figure 1a) has an area of about 68 km^2 (MacMahan et al., 2014). About 3 km upstream from the mouth, the inlet intersects the Intracoastal Waterway (ICW), which connects to other inlets, including Browns Inlet 12 km to the north (Figure 1a) and New Topsail Inlet 36 km to the south (not shown).

3. Observations

Observations of water depths, waves, and currents were collected nearly continuously during May 2012. Wave heights and tidal elevations were measured at 2 Hz for 3,072 s starting at the top of each hour with pressure gages deployed at 17 sites (Figure 1b, black symbols) near and in the inlet mouth. These sensors were colocated with acoustic Doppler velocimeters (ADVs, Figure 1b, triangles) and with acoustic Doppler current profilers (ADCPs, Figure 1b, circles). At most locations, the pressure gages were buried about 0.10 m below the seafloor to avoid dynamic pressure fluctuations (Raubenheimer et al., 2001). The two most onshore pressure sensors used in the momentum balance (Figure 1b, I_{CH} and M) initially were mounted on the seafloor and then were buried about 0.10 m below the seafloor on 4 May 2012 (the resulting shift in mean pressure was accounted for in the processing so that all pressure data are relative to the survey datum). Retaining the 3 days during which the sensors were unburied does not affect the results.

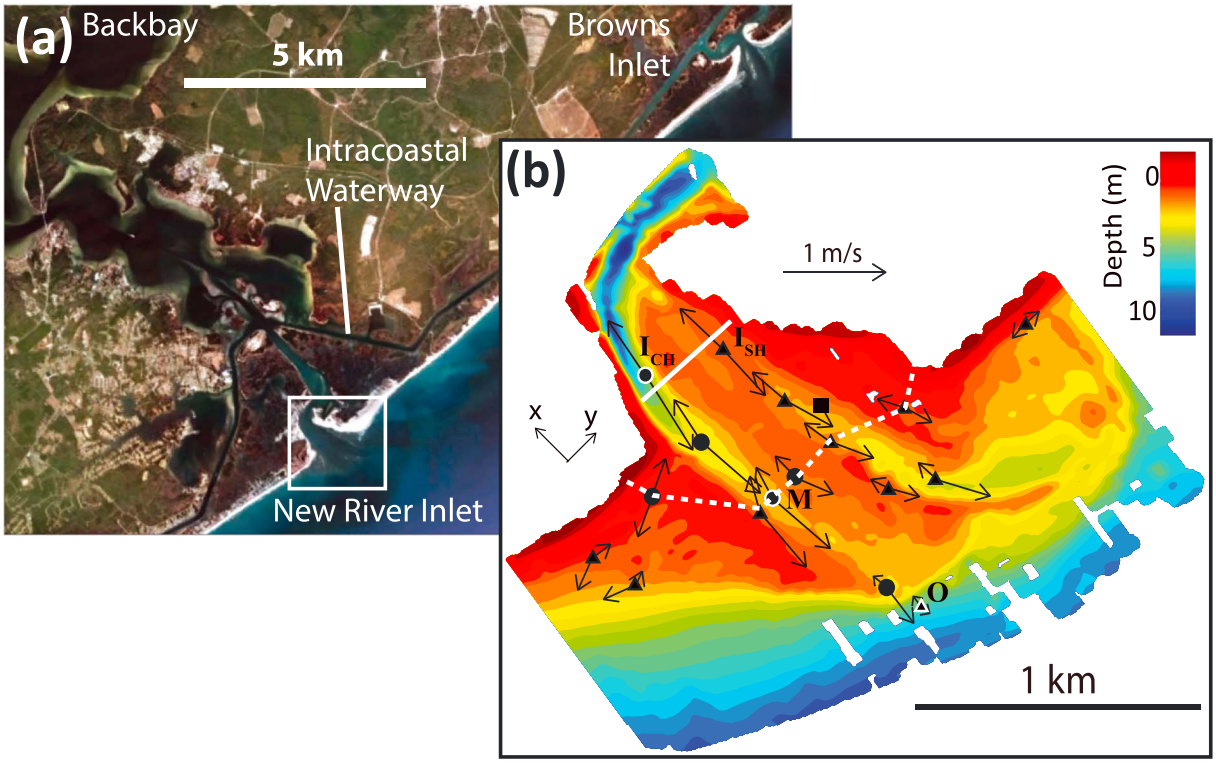

Figure 1. (a) Google Earth image of the North Carolina coast showing New River (inlet and backbay), the Intracoastal Waterway, and Browns Inlet, and (b) close-up view of New River Inlet (white square in Figure 1a) with instrument locations (circles [acoustic Doppler current profilers] and triangles [acoustic Doppler velocimeters] colocated with pressure gages), tidally phase-averaged flood and ebb velocities (black arrows, 1-m/s scale indicated above the contours), and bathymetry (color contours, scale on the right, red is shallow, and blue is deeper water). The black square is the location of Reynolds stress measurements. Measurements used in the momentum balance are from instruments at the three locations labeled O (offshore), M (mid-shoal), and I_{CH} (inlet channel; symbols with white outlines). The solid white line indicates the location of boat-mounted current-profiler measurements, which were used in conjunction with measurements at the instruments marked I_{CH} and I_{SH} (inlet shoals) to estimate inlet discharge. The dashed white curve and the instruments located along it indicate the semicircular region used for observation- and model-based estimates of flows and discharge on the shoal. Cross-shore and alongshore directions are indicated with the black arrows labeled *x* and *y*.

Flows and wave directions were estimated from measurements with ADVs at 11 sites (Figure 1b, triangles), which sampled velocity and pressure at 2 Hz for 3,072 s starting at the top of every hour. The locations of the velocity sample volumes and internal pressure gages for the ADVs were about 0.78 and 0.45 m above the seafloor, respectively. Noisy data from the ADVs (e.g., owing to biofouling or bubbles) were removed (Elgar et al., 2001, 2005). Flows inside the inlet channel (Figure 1b, I_{CH}) were estimated from an upward-looking ADCP, which sampled near-surface flows and near-bed pressure at 2 Hz for 1,024 s starting at the top of the hour and the half hour. In addition, this instrument measured 1-min-averaged current profiles in 0.50-m vertical bins from about 0.70 m above the bed to about 0.50 m below the water surface for 12 min ending on the half hour and hour. Upward-looking ADCPs at other channel locations (Figure 1b, circles, including M) measured 1-min-averaged currents in 0.25-m vertical bins from about 0.45 m above the bed to about 0.25 m below the water surface.

3.1. Waves and Water Levels

Pressure measurements were corrected with atmospheric pressure fluctuations measured at ground level about 5 km inland. Water depths were estimated from the pressure measurements assuming hydrostatic pressure and a water density of 1,026 kg/m^3 (based on salinity of ~36 psu and temperature of ~20 °C measured near the inlet mouth in late April 2012). Mean water depths h were estimated by averaging the data over each 3,072-s record. Water levels η were estimated from the mean water depths and the bathymetry. The water-level fluctuations from the pressure sensors were converted to sea surface elevation fluctuations using linear theory (Raubenheimer et al., 1998). Significant wave heights H_{sig} (Figure 2c) were calculated as 4 times the standard deviation of the sea surface elevation fluctuations in the wind wave frequency f band

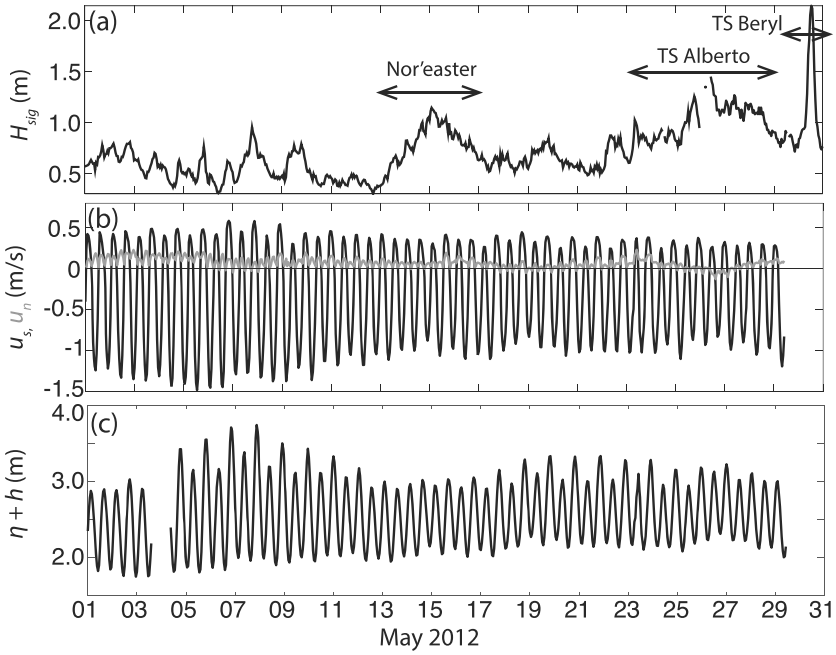

Figure 2. (a) Wave height H_{sig} at the seaward edge of the ebb shoal edge (Figure 1b, O, 6.3-m water depth), (b) depth-averaged cross-shore (u_s, black curve) and alongshore flows (u_n, gray curve) and (c) water levels, (Figure 1b, M) versus time. A nor'easter and named tropical storms are indicated with black arrows.

($0.05 < f < 0.30$ Hz). The estimated wave heights are not sensitive to the low-frequency cutoff, and accounting for wave-current interactions (Smith, 2002) did not significantly affect the wave height or wave forcing estimates. Energy-weighted wave directions in the wind wave frequency band were estimated from the synchronized velocity and pressure measurements (Kuik et al., 1988).

In the southwestern channel (Figure 1b, M), water levels ranged from 1.8 to 3.7 m and differences in successive high and low tides ranged from 0.9 to 1.5 m (Figure 2c). At the edge of the ebb shoal (Figure 1b, O), significant wave heights H_{sig} ranged from 0.5 to 2.5 m (Figure 2a) and centroidal (energy-weighted over the wind wave band) frequencies ranged from 0.11 to 0.18 Hz (not shown). Offshore centroidal wave directions usually were within 20° of the channel axis. During the nor'easter (Figure 2a, 15 May), waves were near shore normal. Refraction (mainly owing to bathymetry) resulted in approximately 10° changes in wave directions around the semicircular ebb shoal. Wave breaking was primarily depth-limited (see Figure 9 in Chen et al., 2015), with small modifications owing to currents (Zippel & Thomson, 2015). Wave heights on the ebb shoal (Figure 1b, M) ranged from 0.0 to 0.7 m (not shown), with average wave heights of 0.2 and 0.4 m on ebb (low tide) and flood (high tide), respectively.

3.2. Flows and Discharge

Time-mean flows were estimated by averaging over the observations in each hour-long period. Hourly averaged current profiles measured with the ADCPs were extrapolated to the bed using a logarithmic fit assuming a no-slip condition and to the surface using a parabolic fit assuming a no-shear condition (Geyer et al., 2000). Mean flows were rotated to cross-shore and alongshore (along-channel and cross-channel; x, y) directions (positive into the inlet and to the northeast), defined by the principal flow axis at the profiler on the ebb shoal (Figure 1b, M), estimated as (Emery & Thomson, 2001):

$$\theta_p = \frac{1}{2}\tan^{-1}\left[\frac{2\langle v'u'\rangle}{\langle v'^2\rangle - \langle u'^2\rangle}\right], \quad (1)$$

where θ_p is the principal axis angle relative to north (clockwise positive), v' and u' are the demeaned north-south and east-west velocity fluctuations, and the brackets $\langle\ \rangle$ indicate time averaging. The resulting major axis angle was 45° counterclockwise of true north (Figure 1b, coordinate system shown on left).

In the southwestern channel on the ebb shoal (Figure 1b, M), tidal currents ranged from −1.5 to 0.6 m/s (Figure 2b). Tidal currents were nearly depth uniform above the bottom boundary layer (not shown). The dominant tidal constituent was the M_2 (12.4 hr semidiurnal lunar) tide. Although New River Inlet is a short channel relative to the tidal wavelength (the ratio of channel length to a quarter of a tidal wavelength is about 0.3; Li & O'Donnell, 2005), the tides are progressive, with peak ebbs (floods) occurring within about 30 min of low (high) water levels (MacMahan et al., 2014). Tidal Stokes drift can be significant over the shallow ebb shoal (section 6.3).

Boat-mounted current profile transects were conducted across the inlet mouth (Figure 1b, white solid line) for 14 hr on 11 and 14 May. The downward-facing profiler was positioned 0.20 m below the water surface and sampled the water column at 1 Hz in vertical bins ranging in size from 0.02 to 0.50 m, with blanking distances of 0.20 to 0.50 m below the sensor, depending on the water depth (measured by a separate vertical acoustic beam) and velocity conditions. Boat velocity and position were measured by GPS with real-time kinematic corrections. The profiling system uses a power law velocity profile (Chen, 1991) to extrapolate the flows to areas above and below the measured profiles. Near-stationary flow measurements were collected and averaged over 120 to 240 s near the inlet edges and used to extrapolate the flow measurements to the shore assuming sloped banks and a visually determined distance. Less than 10% of the total discharge is within the top, bottom, and edge regions, and the estimated discharges from the profiler surveys are not sensitive to the extrapolation methods.

Discharge also was estimated using the inlet bathymetry and the velocities and water levels measured at the two most onshore locations inside the inlet mouth (Figure 1b, I_{CH} and I_{SH}), assuming that the fixed measurements are representative of the southwestern channel and northeastern shoals areas, respectively. The resulting hour-averaged discharge estimates are 10% to 40% larger than those estimated from the boat-mounted profiler (not shown), and the estimated 12-hr averaged discharge is 8% and 18% larger than that estimated from the boat-mounted profiler on 11 and 14 May, respectively. The overestimation using fixed profilers may occur because velocities in shallow regions of the inlet are smaller than those observed at I_{CH} and I_{SH}.

There were large gaps in the observations on the shoals (Figure 1b, I_{SH}) at the beginning of May, and thus discharge was estimated from the fixed sensors for 23 days from 10 May to 1 June. The hour-averaged discharge (the tidal transport) estimated inside the inlet mouth (Figure 1b, I_{CH} and I_{SH}) ranged from −1,200 to 1,600 m^3/s (not shown).

Discharge also was estimated from the observed water depths (the bathymetry and water levels) and flows at six locations around the ebb shoal (Figure 1b, white dashed curve) to compare an overall volume transport estimate with alongshore variability in flows (section 6.3). Flows were extrapolated to the shores and interpolated between the measurements by assuming a balance between pressure gradient and bottom stress, a constant bottom drag coefficient, and a constant sea surface slope along the semicircular cross section, such that $u_2 = u_1\sqrt{(\eta + h_2)/(\eta + h_1)}$ (where η is the water level, u_1 is the velocity measured in water depth h_1, and u_2 is the velocity estimated at a new location with depth h_2). Discharge estimates are not sensitive to the interpolation scheme. Integrating along the curve surrounding the inlet (Figure 1b, white dashed curve), the estimated ebb and flood discharges are similar (maximum estimates were −1,100 and 1,000 m^3/s, respectively, and average discharges over all ebbs and floods were −760 and 600 m^3/s). These discharge estimates are 7% stronger and 23% weaker than the simultaneous discharge (not shown) estimates inside the inlet (Figure 1b, solid white line) on ebb and flood, respectively (within the error of the inlet-discharge estimates). The larger difference on flood may be owing to poor velocity resolution over the shallow areas.

3.3. Other Measurements

Winds were measured (5-min means) from 1 to 21 May with an anemometer about 4.3 m above NAVD88 (approximately mean sea level) in 2-m water depth southwest of the inlet mouth. Hourly offshore winds from a buoy in 10-m water depth (National Data Buoy Center station 41038), 55 km southwest of New River Inlet, were used to extend the data set. The onsite and National Data Buoy Center wind measurements were correlated ($r^2 \sim 0.7$) with 95% confidence. Measured winds were converted to 10-m winds assuming a logarithmic layer, neutral stability, and a roughness length model (Charnock, 1955). Wind speeds ranged from 0 to 16 m/s and wind directions most frequently were from the south or southwest (not shown).

Temperature and salinity were estimated with conductivity-depth-temperature measurements over 6 days at different tidal stages (flood, ebb, and slack; spring and neap) from 3 to 20 May. Density estimated from 39 profiles within 100 m of the profiler on the ebb shoal (Figure 1b, M) ranged from 1,024 to 1,025 kg/m^3 and was nearly vertically uniform (buoyancy frequency $N^2 = O(10^{-9})$ s^{-2}), and thus baroclinic effects on the flows are neglected. Horizontal variability in density (baroclinic forcing) also was negligible.

4. Numerical Model

The model, NearCoM-TVD (Chen et al., 2014, 2015; Shi et al., 2003) couples the spectral wave model SWAN (Booij et al., 1999) with the nearshore circulation model SHORECIRC (Svendsen et al., 2002). The quasi 3-D SHORECIRC is a two-dimensional horizontal model that incorporates the mixing induced by the vertical variation of wave-induced horizontal circulation. The curvilinear model grid extends 40 km offshore to 27-m depth, and alongshore 32 km centered on the inlet, and includes the backbay and the ICW. The digital elevation model (DEM) is comprised of three data sets: the DEM of Onslow Beach and the ICW bathymetry (November 2005, U.S. Army Corps of Engineers [USACE]) combined with Swath bathymetry (August 2008, Virginia Institute of Marine Science), the DEM of the New River backbay from Swath bathymetry (August 2009, USACE), and the DEM of the inlet and the ebb tidal delta (Figure 1b; May 2012, USACE). These three DEMs were combined and interpolated onto the curvilinear grid with 10-m resolution near the inlet and 200-m resolution in the backbay and offshore regions. The model bathymetry was smoothed near the steep channel slopes to ensure stability.

Spatially and temporally dependent tidal forcing is applied on the offshore and alongshore boundaries of the circulation model using the amplitudes and phases of the M_2, S_2, N_2, K_2, O_1, and K_1 tidal constituents provided by the ADCIRC (Luettich et al., 1992) database. The circulation model time step is determined internally to satisfy a Courant condition throughout the domain and is about 1 s. Wave forcing is applied on the offshore boundary of SWAN (in stationary mode) using the significant wave height and peak period reported every 30 min at NOAA station 41036 (25-m depth) and mean wave directions reported at NOAA station 41109 (13-m depth). The NearCoM-TVD model used a depth-limited wave breaking formulation without rollers (Battjes & Janssen, 1978) with the default value $\gamma = 0.73$. Radiation stress is estimated in SWAN from the wave breaking-induced momentum flux (Longuet-Higgins & Stewart, 1964). The wave and circulation models are two-way coupled (SWAN passes wave parameters to SHORECIRC, and SHORECIRC passes water levels and flow velocities to SWAN) and account for wave-current interactions. Bottom friction is modeled using an empirical method (Soulsby et al., 1993) that accounts for bed stresses owing to both waves and currents. The eddy viscosity formulation accounts for mixing owing to wave breaking, bottom-generated turbulence, and subgrid stresses (Nadaoka & Kondoh, 1982; Smagorinsky, 1963; Svendsen, 1987). More details about NearCoM-TVD and the model setup at New River Inlet can be found elsewhere (Chen et al., 2015; Shi et al., 2011; Spydell et al., 2015).

5. Evaluation of Model Momentum Balance

Previous studies have shown that the NearCoM-TVD model simulations reproduce the water levels, waves, and currents observed at New River Inlet reasonably well (sensors O, M, I_{CH}, and I_{SH} are sensors 68, 6, 4, and 54, respectively, in Chen et al., 2015; see also Spydell et al., 2015). Modeled flows in the channel at the mid-shoal location are tidally asymmetric, with ebb flows 3 times stronger than flood flows, similar to the observations. However, the magnitudes of the flows are 20% to 30% weaker in the model than in the observations. Simulated wave heights are 8% larger than the observed wave heights offshore of the ebb shoal and 12% larger than observed during flood on the ebb shoal (Figure 1b, M; both observed and simulated wave heights were small on the ebb shoal during ebb). Although the model reproduces the kinematic quantities reasonably well, small errors can lead to significant differences in the spatial gradients in the momentum balance. Thus, to enable comparison of simulated with observed terms in the momentum balance, the simulated terms are estimated from model output in the same manner as the momentum terms are estimated from the fixed-instrument observations.

5.1. Cross-Shore Momentum Balance

The simulations are compared with the observations using the depth-integrated cross-shore momentum balance:

$$\frac{\partial Hu}{\partial t}+\frac{\partial Hu^2}{\partial x}+\frac{\partial Huv}{\partial y}-fHv=-\frac{H}{\rho_0}\frac{\partial P_b}{\partial x}+\frac{\tau^{sx}}{\rho_0}-\frac{\tau^{bx}}{\rho_0}-\frac{1}{\rho_0}\left[\frac{\partial S_{xx}}{\partial x}+\frac{\partial S_{xy}}{\partial y}\right], \tag{2}$$

where t is time, x and y are the cross-shore and alongshore coordinates (positive into the inlet and to the northeast, Figure 1b, coordinate system on the left), u and v are the depth-integrated cross-shore and alongshore velocities, H is the time-varying water depth ($H=\eta+h$, where η is the time-varying sea surface elevation and h is the time-mean depth), f is the Coriolis parameter, ρ_0 is the time-mean density (1,026 kg/m^3), P_b is the bottom pressure, τ^{sx} and τ^{bx} are the wind and bottom stresses, and S_{xx} and S_{xy} are the cross-shore and diagonal wave radiation stresses. Tidal sea level variations η are significant (tidal amplitude is about a third of the depth in the deep channel, Figure 2c) and cannot be neglected (Lentz et al., 1999).

The bottom pressure P_b is simplified by the constant density hydrostatic equation $P_b=\rho_0 gH$, where g is the gravitational acceleration. Wind stress τ^{sx} is approximated as $\tau^{sx}=\rho_a C_w u_w|U_w|$, where ρ_a is the air density, C_w is the wind drag coefficient (Large & Pond, 1981), and u_w and $|U_w|$ are the cross-shore and total wind speed at 10 m above the water surface. Bottom stress τ^{bx} is approximated with the quadratic drag law $\tau^{bx}=\rho_0 C_D u|U|$, where C_D = 0.005 is the bottom drag coefficient estimated from the Reynolds stress measurements (see Appendix A) and $|U|$ is the total flow speed ($|U|=\sqrt{u^2+v^2}$). Wave-driven enhancement of the bottom drag coefficient (Grant & Madsen, 1979) is negligible (see Appendix A), possibly owing to the small wave heights and significant currents on the ebb shoal. The wave radiation stresses are approximated as (Apotsos et al., 2008; Longuet-Higgins & Stewart, 1964; Raubenheimer et al., 2001):

$$S_{xx}=E_w\left[\left(\cos^2\theta_b+1\right)\frac{c_g}{c}-\frac{1}{2}\right], \tag{3}$$

$$S_{xy}=E_w\cos\theta_b\sin\theta_b\frac{c_g}{c}, \tag{4}$$

where θ_b is the centroidal wave direction (relative to the along-channel direction), c_g and c are the wave group and phase speeds (estimated from the centroidal frequency and the water depth), and E_w is the wave energy, calculated as

$$E_w=\frac{1}{16}\rho_0 g H_{sig}^2. \tag{5}$$

The results are not sensitive to the roughly 10% to 15% overestimation during large wave events of radiation stresses estimated using the bulk formulae (equations (3) and (4)) relative to those estimated using a frequency-dependent directional moment technique (Elgar et al., 1994; Feddersen, 2004; Herbers & Guza, 1990; Raubenheimer et al., 2001). Coriolis acceleration is neglected because it is small ($O(10^{-5})$ m^2/s^2) and the Rossby number ($U/(fL)\approx 10$, where U is the flow speed at the inlet [1 m/s], f is the Coriolis parameter [8×10^{-5} 1/s at 35° latitude], and L the inlet width [1,000 m]) is large at the inlet. Wind stress is small ($O(10^{-5}$ to $10^{-4})$ m^2/s^2) relative to the other terms and is neglected. Owing to the O(100 m) alongshore (cross-channel) variability in bathymetry and the large horizontal separations between instrument locations (>500 m), alongshore gradients in the momentum terms ($\partial/\partial y$) cannot be estimated from observations.

Thus, a simplified momentum balance is used to compare observations with simulations:

$$\frac{1}{H}\frac{\partial Hu}{\partial t}+\frac{1}{H}\frac{\partial Hu^2}{\partial x}=-g\frac{\partial \eta}{\partial x}-\frac{C_D u|U|}{H}-\frac{1}{\rho_0 H}\frac{\partial S_{xx}}{\partial x}, \tag{6}$$

where, from left to right, the terms are the local acceleration, cross-shore advection, barotropic pressure gradient, bottom stress, and cross-shore wave radiation stress gradient.

5.2. Model-Data Comparison

To validate the simulations with the observations, momentum balance terms are estimated from the kinematic model results using the same methods and sensor locations as used for the observations. Thus, in the comparisons here, simulation- and observation-based momentum balance terms are estimated from the hour-averaged water depth, waves, and currents. Simulated velocities and depths were averaged over

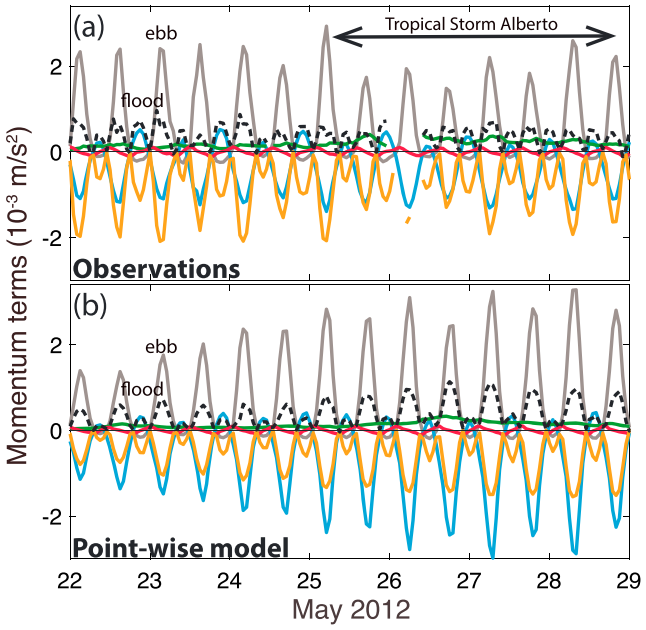

Figure 3. Depth-averaged, cross-shore momentum balance terms estimated from the (a) observations and (b) simulations versus time. The momentum balance terms are pressure gradient (blue curve), bottom stress (gray curve, positive values indicate offshore-directed flows), wave radiation stress gradient (green curve), cross-shore advection (orange curve), local acceleration (red curve), and residual (black dashed curve). The squared correlation r^2 between observed bottom stress and pressure (Figure 3a) is 0.87 ± 0.06, and r^2 between bottom stress and the sum of all the other terms is 0.95 ± 0.03. Correlations between momentum terms estimated from the simulations (Figure 3b) are qualitatively similar.

nine grid points (30- to 50-m radius) surrounding each sensor location to smooth spatial variability. The relative magnitudes of the terms are similar with or without spatial averaging.

Gradients are estimated as the forward difference between sensors seaward of the ebb shoal edge and inside the inlet (Figure 1b, O to l_{CH}), divided by the straight-line distance between the sensors ($\partial x \approx 1{,}300$ m). The results are qualitatively similar between O and the sensor midway between M and l_{CH} (Figure 1b).

Observed and simulated bottom stress is tidally asymmetric (larger on ebb) and correlated with the pressure gradient (Figures 3 and 4, gray and blue curves; and Figures 5a and 5d). Local acceleration (Figures 3 and 4, red curve) is negligible, except near slack tide. The pressure gradient is significantly larger on ebb than on flood (Figures 3 and 4, blue curves; and Figures 5a and 5d), which may be owing to the larger force needed to drive the discharge through the 40% smaller ebb cross-sectional area (see section 6.3). However, bottom stress is more tidally asymmetric (has a larger flood-ebb inequality) than the pressure gradient (Figures 3 and 4, compare gray with blue curves), suggesting other momentum terms contribute to flow asymmetry.

Cross-shore advection (Figures 3 and 4, orange curves) arises from spatially decelerating and accelerating flows on ebb and flood, respectively. Without considering advection, bottom stress is stronger (weaker) than the pressure gradient on ebb (flood; Figures 5a and 5d, *y* axes values are smaller [larger] than the 1:1 line). Advection is a source of momentum on ebb (compare Figure 5a with 5b and Figure 5d with 5e, advection increases the magnitude of *y* axis terms [blue circles]), and advection is a sink of momentum on flood (compare Figure 5a with 5b and Figure 5d with 5e, advection decreases the magnitude of *y* axis terms [red circles]), enhancing tidal asymmetry.

Cross-shore advection degrades the correlation and increases the error in the simplified momentum balance on flood (compare the flood [red] legends in Figures 5a and 5d with those in Figures 5b and 5e) and has a

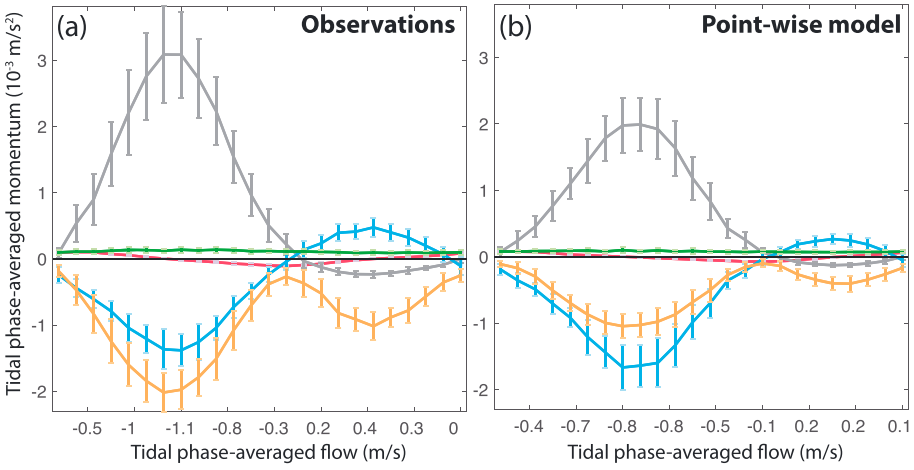

Figure 4. Tidal phase-averaged momentum balance terms for (a) observations and (b) pointwise model estimates versus tidal phase-averaged cross-shore flows. The terms and flows were phase-averaged using the M_2 tidal flow frequency, which was extracted with a harmonic analysis. The momentum balance terms are pressure gradient (blue curve), bottom stress (gray curve, positive values indicate offshore-directed flows), wave radiation stress gradient (green curve), cross-shore advection (orange curve), and local acceleration (red curve). Vertical bars are one standard deviation.

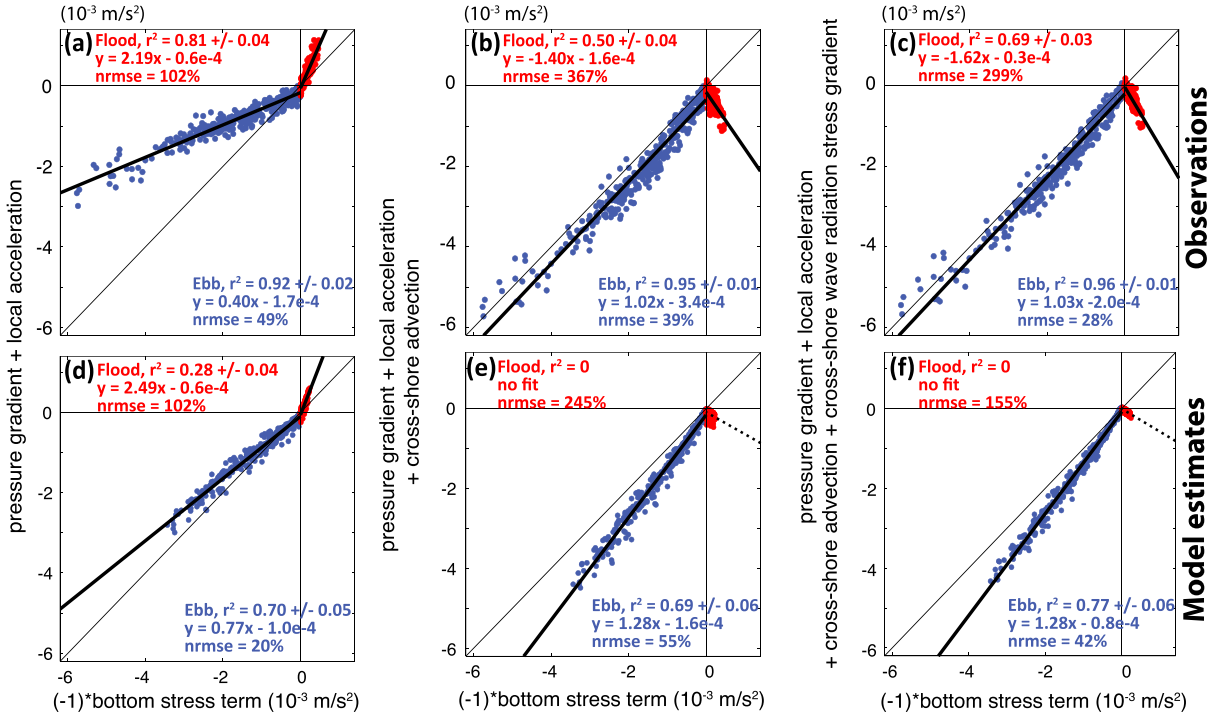

Figure 5. Depth-averaged, cross-shore momentum balance terms from (a–c) observations and (d–f) model outputs at sensor locations versus negative bottom stress term for flood (red circles) and ebb (blue circles). The panels are the sum of (a, d) pressure gradient and local acceleration, (b, e) pressure gradient, local acceleration, and cross-shore advection, and (c, f) pressure gradient, local acceleration, cross-shore advection, and wave radiation stress gradients. The thin diagonal lines have a slope of 1, and the thick diagonal lines are the least squares fits (given on each panel, along with the correlation coefficient r^2). The normalized (by bottom stress) root-mean-square error of each balance is given for flood and ebb. The root-mean-square error (not normalized) and mean normalized error (not shown) are similar. Model-based results (d–f) are shown only for times with corresponding observations.

negligible effect on the correlation on ebb (compare the ebb [blue] legends in Figures 5a and 5d with those in Figures 5b and 5e). The large errors on flood may be owing to inaccuracies in estimating the cross-shore advection. Cross-shore advection estimated from the mid-shoal (Figure 1b, M) to inside the inlet (Figure 1b, I_{CH}) on flood (ebb) is an order of magnitude (60%) larger than that estimated from the offshore (Figure 1b, O) to the mid-shoal (Figure 1b, M) locations. Thus, the majority of the cross-shore spatial acceleration of flow is concentrated between the mid-shoal and the inlet mouth on flood, whereas flows spatially decelerate more uniformly across the ebb shoal on ebb. The inequality in advection onshore and offshore of the mid-shoal on flood suggests the first-order forward differencing method (which assumes a constant gradient) does not estimate the gradient accurately at mid-shoal (Figure 1b, M), and thus the cross-shore advection may be overestimated significantly on flood. In addition, owing to the convergence of the flows entering the constriction, the alongshore (cross-channel) advection term may be important to the dynamics on flood, but it is neglected here (see Appendix B).

The wave radiation stress gradient (Figures 3 and 4, green curves) is small, except on flood during storms. Including wave forcing in the momentum balance reduces scatter (Figures 5c and 5f) and enhances flood flows (reduces the negative *y* intercepts for the observations). Although alongshore wave radiation stress gradients (neglected in this analysis) could not be estimated with this observation-based method, these terms are expected to be smaller than the cross-shore wave forcing.

The model reproduces the time-varying variability in momentum reasonably well (Figure 3). The tidal asymmetry of the magnitude of the simulated momentum terms is larger than observed (Figure 3), suggesting larger tidal asymmetry in the simulated flows (bottom stress) and gradients of flows and water levels (advection and pressure gradient). The model also has a stronger spring-neap modulation than observed (compare simulated [Figure 3b] neap [22 May] and spring [27 May] tidal amplitudes with the observed amplitudes [Figure 3a]). This difference partially may explain the difference between the average simulated

momentum terms and the larger corresponding terms estimated from the observations (compare *x* and *y* ranges of the symbols in Figures 5a and 5c with those in Figures 5d and 5f). The correlations between the simulated momentum terms and bottom stress (legends in Figures 5d and 5f) are lower than the correlations between the observed terms and bottom stress (legends in Figures 5a and 5f), possibly owing to the method used to average over grid cells near the in situ sensors and to the stronger spring-neap cycle in the model.

The relative importance of the simulated momentum terms (Figure 4b) on flood and ebb is similar to that observed (Figure 4a). Although the simulated water levels and flows agree reasonably well with the observations (Chen et al., 2015), on flood (Figure 4, positive *x* axis values) the errors result in a 50–60% underestimation of the observed pressure gradient (compare blue curve in Figure 4a with the blue curve in Figure 4b), advection (orange curves), and bottom stress (gray curves). On ebb (Figure 4, negative *x* axis values), the simulated pressure gradient is 20% larger (compare blue curve in Figure 4a with the blue curve in Figure 4b), and the simulated advection (orange curves) and bottom stress (gray curves) are 50% and 30% smaller than observed, leading to a change in the relative importance of pressure gradient and advection. During both flood and ebb, simulated wave radiation stress gradients (Figure 4b, green curve) are 20–30% weaker than observed (Figure 4a, green curve).

Although the simulated momentum estimates differ quantitatively from the observed estimates, the trends qualitatively are similar, and thus the model can be used to investigate the cross-shore dynamics and wave effects.

6. Results

The role and cross-shore variability of each of the terms in the momentum balance is examined along the southwestern channel using the direct model outputs. The terms in the simulated momentum balance were averaged over 100-m diameter regions (Figure 6a) to reduce spatial variability. The simulated depth-integrated momentum terms were divided by the average depth in the 100-m diameter region. Results are similar without spatial averaging. The modeled total advection and wave radiation stress gradients include both cross-shore and alongshore contributions, which could not be separated owing to the curvilinear grid. The model balance between pressure gradient, local acceleration, total advection, total wave forcing, and bottom stress has less than 3% residual (not shown) owing to neglected momentum terms (Coriolis acceleration, wind stress, horizontal diffusion, and 3-D dispersion effects induced by the vertical variation of horizontal velocities [Putrevu & Svendsen, 1999]), conversion from a curvilinear coordinate system, and spatial averaging methods.

The model was run with and without wave forcing at the offshore boundary (with the same tidal forcing for the same month-long period) to evaluate the effects of waves on the momentum balances. The analysis focuses on three regions extending from the shoal edge to inside the inlet mouth (Figure 6). The shoal edge ($0 < X_{cs} < 550$ m) is the region where the pressure gradient associated with wave breaking-induced setup is greater than the tidal pressure gradient, the mid-shoal ($550 < X_{cs} < 850$ m) is the region where the tidal pressure gradient is greater than the setup, and the inlet ($850\ \text{m} < X_{cs}$) is the region onshore of the mouth.

6.1. Simulated Cross-Shore Variability in Momentum Balances With and Without Waves

In the absence of waves, bottom stresses and pressure gradients on the shoal edge are ebb dominated (compare magnitudes of gray and blue dashed curves in Figure 6c with those in Figure 6b). Advection is similar in magnitude, but opposite in sign, to the pressure gradient on flood (Figure 6b, dashed orange curve, advection is a sink of momentum [pressure gradient acts to accelerate the flows and overcome bed stress]). Although advection is small on ebb, it adds to the pressure gradient (Figure 6c, dashed orange curve, advection is a source of momentum [same sign as pressure gradient, which combined with the flow inertia are balanced by the bed stress]). In the absence of waves, there is similar tidal asymmetry owing to advection at the shoal edge and mid-shoal (not shown). Advection changes sign inside the inlet (dashed orange curve at $X_{cs} > 1{,}000$ m in Figure 6b and $X_{cs} > 750$ m in Figure 6c), possibly owing to changes in channel depth and width.

The wave radiation stress gradient is largest at the shoal edge, decays rapidly over the mid-shoal as waves break, and is negligible inside the inlet (Figures 6b and 6c, green curves). There is tidal variability in the cross-shore location of wave breaking (Figures 6b and 6c, green curves are maximum at cross-shore

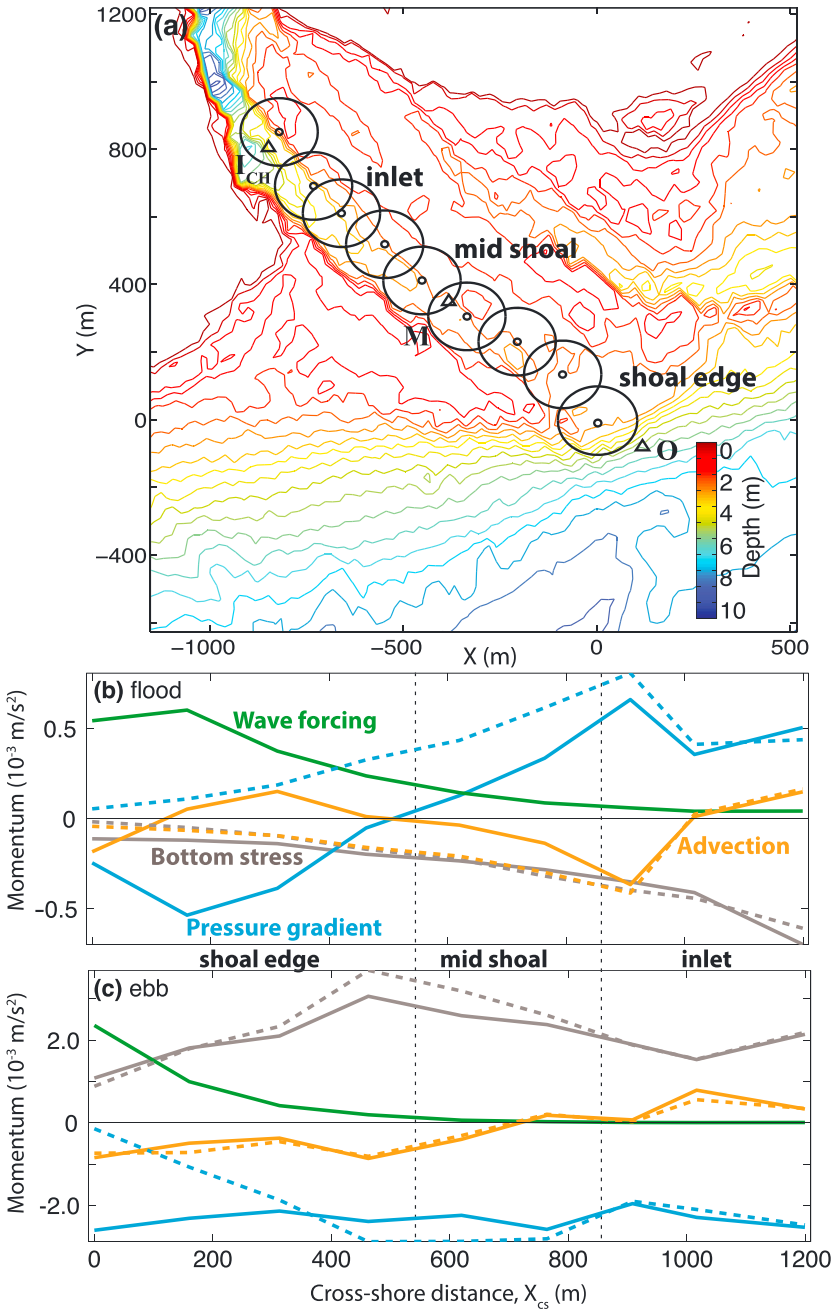

Figure 6. (a) Locations of simulated momentum outputs averaged over 100-m diameter regions (large circles) and of the sensors (triangles, see also Figure 1b, O, M, l_{CH}) used in the observation-based momentum estimates overlaid on bathymetry contours (scale on right). Pressure gradient (blue curves), bottom stress (gray curves, positive values indicate offshore-directed flows), total advection (orange curves), and total wave radiation stress gradient (green curves) averaged over (b) flood (26 May) and (c) ebb (30 May; when observed $H_{sig} > 1.2$ m) for model runs with (solid curves) and without (dashed curves) waves versus cross-shore distance, X_{cs} (where 0 m is near the ebb shoal edge, same as $X = 0$ and $Y = 0$ in Figure 6a, and distance is positive onshore). Note that offshore is to the right of Figure 1a and to the left of Figures 1b and 1c.

distances of 180 and 0 m, respectively), mainly owing to the tidal change in water depth (deeper on flood; Chen et al., 2015).

Large offshore waves ($H_{sig} > 1.2$ m) drive changes to the pressure gradient across the shoal edge and mid-shoal regions (Figures 6b and 6c, compare dashed with solid blue curve). At the shoal edge, the change in

the pressure gradient term is similar in magnitude to the wave forcing term, suggesting that these changes are mainly owing to local wave-driven changes to the water levels (setdown and setup, see section 6.2). At the shoal edge, including wave forcing causes the pressure gradient to become negative on flood (offshore directed; Figure 6b, solid blue curve is negative for $X_{cs} < 500$ m) and to become more negative on ebb (Figure 6c, compare dashed with solid blue curve for $X_{cs} < 300$ m), consistent with wave-enhanced offshore-directed water level gradients. On the mid-shoal, the pressure gradient is decreased on flood and ebb (water levels are less steep) during large waves (Figures 6b and 6c, compare dashed with solid blue curves for ~$400 < X_{cs} \sim 700$ m). These changes in pressure gradient are larger than the magnitude of the local wave forcing term (i.e., not in balance), suggesting that waves may have a nonlocal effect on the water levels in this region (see section 6.2).

During flood, along most of the ebb shoal the overall forcing (the sum of wave forcing and pressure gradient) is weaker with large waves (less net force driving water toward the inlet) than in the simulations without waves (Figure 6b, ~$100 < X_{cs} \sim 900$ m). During ebb, the overall forcing is not affected by waves, except in the mid-shoal region (Figure 6c, ~$400 < X_{cs} < \sim 700$ m), where the forcing is weaker with large waves (less net force driving water away from the inlet) than without waves.

Waves mainly affect the spatial gradients of circulation (advection) on flood and the local circulation (bottom stress) on ebb (Figure 6). During flood, bottom stress is not affected by waves (Figure 6b, compare dashed with solid gray curve). In contrast, compared with no waves, with large offshore waves ($H_{sig} > 1.2$ m) advection changes sign at the shoal edge (Figure 6b, solid orange curve, $100 < X_{cs} < 400$ m) and decreases on the mid-shoal (Figure 6b, compare dashed with solid orange curve, $550 < X_{cs} < 850$ m). This change in advection suggests that the response of the circulation to waves on flood primarily is a change in the spatial gradients of the flows (i.e., convergences or divergences). On ebb, advection is not affected by waves (Figure 6c, compare dashed with solid orange curve), whereas bottom stress on the mid-shoal is decreased with large waves (Figure 6c, compare dashed with solid gray curve, $200 < X_{cs} < 700$ m). A decrease in bottom stress is consistent with a local change in water level and flows with large waves on ebb. The tidal asymmetry in the flow response to waves (a change in spatial gradients on flood and a change in local kinematics on ebb) leads to different flow asymmetry in the channel during storms than during periods without waves (see sections 6.2 and 6.3).

6.2. Local and Nonlocal Wave Effects

Here the simulations with and without waves are used to examine how water levels and cross-shore flows along the deep southwestern channel on the ebb shoal (Figure 6a, black circles) respond to large offshore wave events ($H_{sig} > 1.2$ m).

Local (direct) and nonlocal (indirect) wave-driven processes induce changes in the water levels on the ebb shoal (Figure 7a, solid curves). Shoaling and breaking waves locally drive changes to the water levels through setdown (Figure 7a, solid red curve is less than 0 at cross-shore distance ≈ 0 m) and setup (Figure 7a, solid blue and red curves are positive owing in part to setup). In addition, onshore mass transport is enhanced (Orescanin et al., 2014; Wargula et al., 2014) and the ebb jet is partially blocked (Olabarrieta et al., 2014) owing to wave radiation stress gradients (or wave breaking-induced accelerations), leading to a nonlocal (i.e., local wave heights are negligible, not shown) wave-driven increase in water levels (relative to tidal levels) near and inside the inlet (Figure 7a, solid red and blue curves are positive).

The response of flows to large offshore wave events is complex and nonlinear (Figure 7b, solid curves). In particular, waves may drive changes to the flows through several local (direct) and nonlocal (indirect) processes, including wave radiation stress gradients, wave-driven changes to the pressure gradient, wave-driven changes to the local water levels (the momentum owing to bottom stress is a function of velocity and water level), and horizontal variability in wave effects (advection is proportional to velocity and a horizontal length scale, i.e., cross-shore and alongshore spatial gradients of the circulation). For the conditions here the direct wave effects on flows through the breaking wave-induced changes to the bottom stress are small (see Appendix A).

At the shoal edge, local wave radiation stress gradients are large and drive significant changes to the local pressure gradient (Figures 6b and 6c, blue and green curves). However, on ebb, the net force (the sum of wave radiation stress gradient and pressure gradient, not shown) is similar between simulations with and without waves, leading to negligible changes in the bottom stress and advection (Figure 6c, gray and

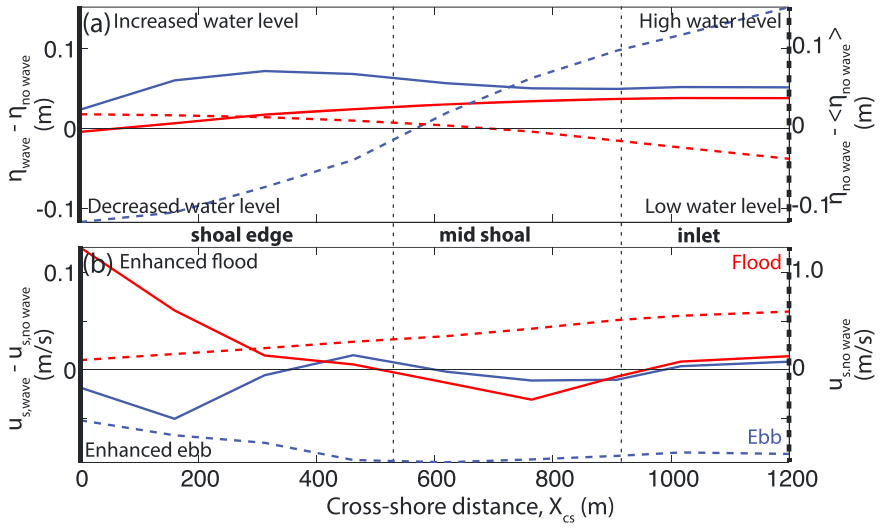

Figure 7. Simulated (a) wave-driven change in sea surface level $\eta_{wave} - \eta_{no\ wave}$ (water levels from the case with waves minus water levels from the case without waves; solid curves, axis on the left) and tidal sea surface level $\eta_{no\ wave} - <\eta_{no\ wave}>$ (de-meaned cross-shore water levels for the case without waves; dashed curves, axis on the right) and (b) wave-driven cross-shore flows $u_{s,wave} - u_{s,no\ wave}$ (flows from the case with waves minus flows from the case without waves; solid curves, axis on the left) and tidal cross-shore flows $u_{s,no\ wave}$ (flows from the case without waves; dashed curves, axis on the right) versus cross-shore distance, X_{cs}. Results have been averaged over maximum floods (red curves) and ebbs (blue curves) during times with offshore wave heights greater than 1.2 m (Figure 2a).

orange curves for $X_{cs} < 350$ m). Thus, the enhancement of cross-shore ebb flows at the shoal edge (Figure 7b, solid blue curve is negative for $X_{cs} < 350$ m) may be owing to the increase in local water levels (the momentum owing to bottom stress is a function of U^2/D, where U is a velocity scale and D is a depth scale). On flood, the cross-shore flows toward the inlet are enhanced at the shoal edge (Figure 7b, solid red curve is positive for $X_{cs} < 500$ m), potentially owing to two different mechanisms. On the offshore edge of the shoal edge (Figure 7b, cross-shore distance <200 m), the net force (the sum of wave radiation stress gradient and pressure gradient, not shown) is increased relative to no-wave conditions owing to large wave radiation stress gradients, which enhance local onshore flows. On the onshore half of the shoal edge (Figure 7b, $200 < X_{cs} < 500$ m), the net force on the flows is near zero (not shown) suggesting that wave radiation stress and pressure gradients locally balance. In this region, the enhanced onshore flows (Figure 7b, solid red curve is positive at $200 < X_{cs} < 500$ m) mainly are owing to the inertia of the flows (Figure 6b, solid orange curve is positive at $200 < X_{cs} < 500$ m, suggesting deceleration as inertia drives flows toward the inlet mouth). Overall, these onshore wave-driven flows lead to a reduction in the ebb dominance of the currents and flux at the shoal edge (not shown).

Although the wave radiation stress gradients and cross-shore wave-driven changes to the pressure gradients are negligible inside the inlet (Figures 6b and 6c, green and blue curves, and Figure 7a, solid red and blue curves are flat, $X_{cs} > 900$ m), there is a reduction in ebb dominance during large waves owing to enhanced flood flows and reduced ebb flows (Figure 7b, solid red and blue curves are positive for $X_{cs} > 1{,}000$ m). Relative to simulations without waves (not shown), large waves ($H_{sig} > 1.2$ m) lead to a 5% to 13% increase in the integrated volume transport into the inlet on flood and a 2% decrease in the integrated volume transport out of the inlet on ebb. These results are consistent with previous studies suggesting that large offshore waves lead to enhanced onshore mass flux (Orescanin et al., 2014; Wargula et al., 2014) and the partial blocking of the ebb jet by wave breaking-induced acceleration (Olabarrieta et al., 2014).

The tidal asymmetry and wave-driven responses of an alongshore transect of mid-shoal flows are discussed further using a simple conceptual model (Stommel & Farmer, 1952) in sections 6.3.

6.3. A Conceptual Kinematic Model for Tidal Flow Asymmetry

The preceding analysis of the observations and simulations suggests that bed stresses and pressure gradients are ebb dominant and that advection is an important sink (source) of momentum on flood (ebb) within the

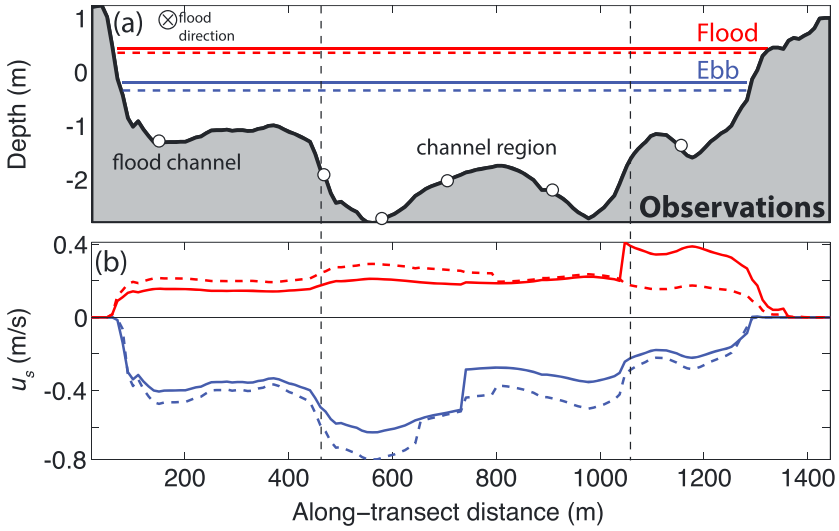

Figure 8. (a) Observed water levels η (colored lines) and water depth h (thick black curve) and (b) observed and interpolated streamwise flows u_s versus along-transect distance (0 m is at the southwestern edge of the inlet, dashed white curve in Figure 1b, flood direction is into the page) averaged over flood (red curves) and ebb (blue curves) during offshore wave heights less than 0.5 m (dashed curves) and greater than 1.2 m (solid curves), excluding the large spring tides (results are similar including spring tides). Open circles are sensor locations. Vertical dashed lines outline the channel region. The ebb shoal current profiler used in the momentum balance (Figure 1b, M) is at along-transect distance = 580 m.

deep southwestern channel (Figures 3–6). Tidal flows also are ebb dominant (Figure 2b and compare flood and ebb arrow lengths in Figure 1b), but waves enhance onshore mass flux into the inlet through both local and nonlocal effects (Figure 7). To examine further the role of the waves and flows over the entire shoal system near the inlet, a simple conceptual model (Stommel & Farmer, 1952) for the two-dimensional horizontal flow patterns is evaluated using observations and model outputs.

Inflow and outflow discharge Q at a constriction are represented conceptually (Stommel & Farmer, 1952) by a semicircular region of uniform flow on flood ($Q_f = \pi b h_f u_f$, where b is the radius of the semicircular region, and h_f and u_f are the water depth and flow speed on flood) and a jet-like region of flow on ebb ($Q_e = a h_e u_e$, where a is the jet or channel width and h_e and u_e are the water depth and flow speed on ebb in the jet or channel area). The average observed discharge was -50 m^3/s, less than 5% of the maximum tidal transport, suggesting that residual discharge owing to export from upstream rivers and exchange with other inlets is negligible. Thus, assuming zero net discharge ($Q_f = Q_e$), flow asymmetry arises from tidal differences in the flow width (πb and a) and depth (h_f and h_e; i.e., and thus $u_e/u_f = \pi b h_f / a h_e$).

Consistent with the conceptual representation (Stommel & Farmer, 1952), the observed (interpolated between sensors, section 3.2) flows roughly are spatially uniform on flood and are concentrated in the main channel on ebb (Figure 8b). Nearly two thirds of the flood flows and only one third of the ebb flows surrounding the inlet vary by less than ±20% from the semicircular cross-sectional average (0.2 m/s on flood and -0.4 m/s on ebb; Figure 8b, dashed red [flood] and dashed blue [ebb] curves, the $H_{sig} < 0.5$-m results are representative of the overall average). Ebb flows in the main (southwestern) channel were twice the cross-sectional average, suggesting significant channelization (Figure 8b, peak in dashed blue curve at along-transect distance of 580 m). The simulated flows (Figure 9b) taken from the same sensor locations (Figure 1b, white dashed curve), averaged spatially over the neighboring grid points, and interpolated with the same methods (section 3.2) have similar variability on flood and ebb, where nearly 50% of the flows vary by less than ±20% from the semicircular cross-sectional average (0.2 m/s on flood and -0.6 m/s on ebb). Ebb flows in the main (southwestern) channel were 1.5 times the cross-sectional average, suggesting channelization (Figure 9b, peak in dashed blue curve at 500 $<$ along-transect distance $<$ 700 m).

The conceptual representation (Stommel & Farmer, 1952) is applied using the depth and velocity averaged in time around maximum flood and ebb (slack tide is excluded by only evaluating times when the

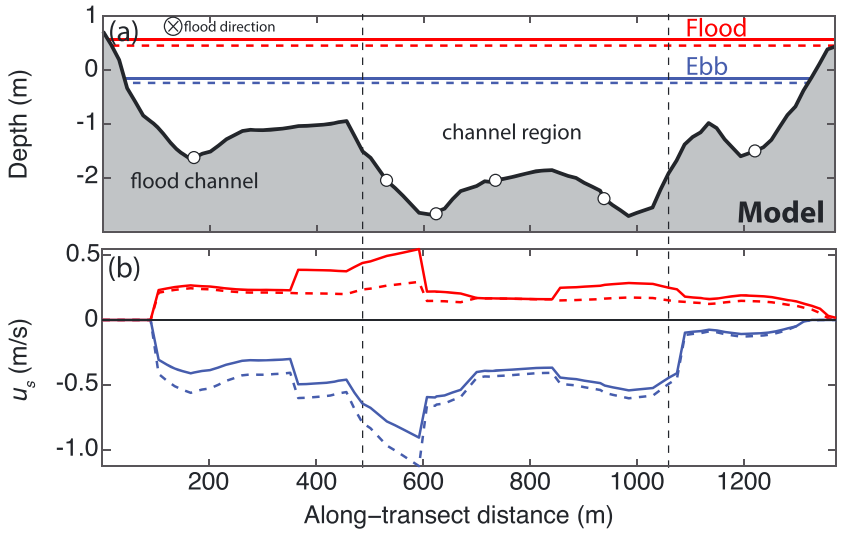

Figure 9. (a) Observed water levels η (colored lines) and water depth h (thick black curve) and (b) simulated streamwise flows u_s versus along-transect distance (0 m is at the southwestern edge of the inlet, dashed white curve in Figure 1b, flood direction is into the page) averaged over flood (red curves) and ebb (blue curves) during offshore wave heights less than 0.5 m (dashed curves) and greater than 1.2 m (solid curves), excluding the large spring tides (results are similar including spring tides). Open circles are sensor locations. Vertical dashed lines outline the channel region. The ebb shoal current profiler used in the momentum balance (Figure 1b, M) is at along-transect distance = 620 m.

instantaneous discharge is greater than the time-average discharge for the full record) and averaged in space over the semicircular region surrounding the inlet (which has a radius b of about 500 m, half the width from shore to shore of the inlet mouth) on flood and in the channel region (Figures 8 and 9, between vertical dashed lines) on ebb. On flood, the average (including all wave conditions) depth and velocity is h_f = 1.8 m and u_f = 0.2 m/s for observations (h_f = 2.0 m and u_f = 0.2 m/s for simulations). On ebb, the average depth and velocity (including all wave conditions) is h_e = 1.9 m and u_e = −0.5 m/s for observations (h_e = 2.0 m and u_e = −0.6 m/s for simulations). The channel width a including the intervening shoals is approximately 600 m (~475 < along-transect distance < ~1,050 m, Figures 8a and 9a). The flood (h_f) and ebb (h_e) depths are nearly equal despite the progressive tide (maximum flood flows occur at maximum tidal elevation) because during flood the depth used in the conceptual model is averaged across the semicircular cross section, whereas during ebb, the depth is averaged only over the channel region.

Discharge estimated from observations using this conceptual representation (Stommel & Farmer, 1952) overestimates flood discharge (estimated along the dashed white curve in Figure 1b) by 5% and underestimates ebb discharge by 20%. The lower percentage of ebb flux may be owing to leakage of the ebb flows to areas outside the channel region, particularly through the shallow flood channel at the southwestern corner of the inlet mouth (Figure 8, along-transect distance ≈ 150 m). This leakage would result in reduced ebb-flow dominance in the channel region compared with that expected from the conceptual representation of a single jet on ebb. Discharge estimated from simulations using this conceptual representation overestimates flood discharge by 10% and underestimates ebb discharge by 16%, similar to the discharge estimated from the observations using the conceptual representation. Thus, the Stommel-Farmer conceptual model of nearly uniform inflow on flood and a concentrated jet on ebb describes the tidal asymmetry to first order in the main channel across the ebb shoal (Figure 1b, M).

There may be other contributions to tidal flow asymmetry. On the ebb shoal (Figure 1b, M), the Stokes drift associated with the progressive tidal wave (deeper water at peak flood) leads to a tidally averaged flood-dominant velocity of 0.08 m/s, roughly 25% of the ebb-dominant Eulerian mean velocity. In addition, in the absence of a constriction, alongshore variability in bathymetry can lead to higher friction over the shallow regions compared with that in the channel, resulting in enhanced ebb flows in the channel and enhanced flood flows on the shoals (Blanton et al., 2002; Li & O'Donnell, 1997, 2005). Overtides owing to nonlinearity

enhance tidal asymmetry (Friedrichs & Aubrey, 1988). At New River Inlet, the M_4 overtide is 9% of the M_2 tide on the ebb shoal (Figure 1b, M) and slightly enhances ebb flows in the channel. However, these processes are secondary to the change in flow surface area ($\pi b/a \gg 1$; Stommel & Farmer, 1952) in driving tidal flow asymmetry.

Spatial and tidal variability in water depth can lead to complex wave breaking patterns (Kang & Di Iorio, 2006; Zippel & Thomson, 2015) that drive asymmetric changes to the water levels and flows (Chen et al., 2015; Olabarrieta et al., 2011, 2014; Piedracoba et al., 2005). In particular, as the offshore wave height increases, the observed ebb flows become more uniform spatially (Figure 8, compare solid with dashed blue curve). The root-mean-square (rms) difference between the observed ebb flows along the transect and the observed cross-sectional average ebb flow for waves less than 0.5 m and greater than 1.2 m was 0.27 and 0.17 m/s, respectively, suggesting a decrease in along-transect variability (reduced ebb jet channelization) in the observed ebb flows owing to waves. The rms difference between the observed flood flows along the transect and the cross-sectional average flood flows was 0.06 and 0.07 m/s, respectively. Simulations also show small wave height-related changes in overall lateral variability of the flows for flood and ebb. The rms difference between the simulated ebb (flood) flows along the transect and the simulated cross-sectional average ebb (flood) flows was 0.29 and 0.24 m/s (0.07 and 0.12 m/s) for waves less than 0.5 m and greater than 1.2 m, respectively.

The conceptual model indicates that the ebb-dominance of the flows in the channel region of New River is driven primarily by the tidal variability in flow surface area ($\pi b/a \gg 1$; i.e., ebb flow channelization) and the amount of leakage through the flood channel. In addition, waves may drive small changes to the tidal asymmetry of the flows.

7. Discussion: Model-Observation Comparisons on the Mid-Shoal

Observations and simulations agree well on the dominant dynamics of tidal flow asymmetry at New River Inlet. Advection (section 6.1) and ebb jet channelization (section 6.3) are dominant drivers of the tidal flow asymmetry, suggesting the importance of two-dimensional processes to inlet exchange. In addition, the observations and model suggest that waves can drive changes to the tidal flow asymmetry through feedbacks between local (e.g., wave breaking-induced accelerations) and nonlocal (e.g., wave-driven changes to the sea surface gradients across the ebb shoal) processes (sections 6.1 and 6.2). Although there are differences in the spatial variability of the flow response to waves (e.g., the importance of wave-driven reduction of the ebb jet channelization, section 6.3) in the observations and simulations, both suggest a tidal and spatially variable response to wave effects on the ebb shoal that results in an overall enhanced mass flux into the inlet (Wargula et al., 2014).

Similar to a previous study at this site (Wargula et al., 2014), the model suggests enhanced flood and reduced ebb discharge into the inlet (Figure 7b, $X_{cs} \sim 1{,}200$ m, and Figure 9b) owing to waves. Observations at the six measurement locations across the ebb shoal also suggest that waves cause an overall decrease in ebb flows (Figure 8b). However, simulations with and without waves showed that waves resulted in reduced flood and enhanced ebb flows in the deep channel on the mid-shoal (Figure 7b, negative solid red and blue curves, $650 < X_{CS} < 900$ m). Differences between the model outputs with waves and the model outputs without waves during times with offshore wave heights greater than 1.2 m demonstrate that there is large spatial variability in wave effects, with strong ebb reduction and flood enhancement on the shoals and narrower regions with ebb enhancement and flood reduction (not shown). Thus, discrepancies between simulations and observations within the channel (ebb enhancement or reduction) may occur because spatial variability in the flows is not resolved sufficiently by the observations. For example, the observed wave-induced changes to the flows varied significantly between the six measurement locations along the ebb shoal (Figure 8b).

In addition, the effects of waves are difficult to separate from simultaneous low-frequency (subtidal) changes in flows and water levels (Figure 2b), and discharge (possibly owing to exchanges with the ICW). For example, semicircular-averaged simulated flood (ebb) flows for time periods when the observed wave heights were greater than 1.2 m increased (decreased) by 23% (8%) in the simulations without waves and 44% (16%) in the simulations with waves relative to the flows when wave heights were less than 0.5 m (Figure 9b, compare dashed with solid curves for simulation with waves). The results for the simulations without waves have

similar structure (not shown). The results for the simulations without waves suggest that part of the flood enhancement and ebb reduction attributed to waves (in the observation and simulations) is owing to temporal changes between the periods with waves greater than 1.2 m or less than 0.5 m. However, the stronger enhancement of flood flows and reduction of ebb flows for the simulations with waves (compared to that without waves) suggests that waves, in addition to other factors, contribute to the flood enhancement and ebb reduction.

Sources of model error also may arise from the smoothing of the observed bathymetry to reduce spurious circulation (the model assumes gradual spatial changes; Chen et al., 2015; Feddersen et al., 2016; Rogowski et al., 2014), unresolved vertical variability in flows (Spydell et al., 2015), insufficient blocking of the ebb jet by wave breaking-induced acceleration (Olabarrieta et al., 2014), an overestimation of setup inside the inlet (e.g., owing to unresolved exchanges with the ICW), and an underestimation of wave radiation stress gradients (e.g., owing to incorrectly parameterized dissipation [Ris & Holthuijsen, 1996] and the use of parametric spectra).

8. Conclusions

Observations of water depths, waves, and currents in and near New River Inlet, NC, and simulations from a NearCom-TVD numerical model were used to investigate tidally asymmetric momentum and flows on the ebb shoal offshore of the inlet mouth. The observations and simulations suggest that bed stresses and pressure gradients in the mid-shoal channel are ebb dominant, and that local effects of wave forcing are small. Momentum terms estimated from observed and simulated properties (water levels, flows, and waves) at instrument locations agree reasonable well with each other. Comparison of estimates of the momentum terms from water levels, waves, and currents output by the model at the sensor locations with direct model output of the momentum terms suggests that spatial variability in the cross-shore advection and that alongshore advection may be important to the momentum balance and cannot be estimated accurately from the spatially sparse measurements.

The simulated bed stresses and pressure gradients in the outer and mid-shoal channel are ebb dominant, and the simulated advection is a sink (source) of momentum on flood (ebb). In the absence of waves, the pressure gradient accelerates the channel flows (which are balanced by bed stress) on flood, whereas both flow inertia and the pressure gradient contribute to the channel flows on ebb (the combined effects are balanced by bed stress). In the simulations waves have both local and nonlocal effects, in which the local radiation stress gradient is or is not a significant term in the momentum balance, respectively. In particular, waves drive a (local) setup and enhance onshore mass flux near the shoal edge but also cause increased water levels and onshore mass fluxes inside the inlet where radiation stress gradients are negligible. Both of these wave effects reduce the ebb dominance of the flows.

Consistent with a conceptual representation of an inlet as a constriction that neglects the shoal bathymetry and waves (Stommel & Farmer, 1952), observed and simulated flows on the shoal are jet-like on ebb (in the narrow channels) and nearly are spatially uniform across the wide ebb shoal on flood. This tidal asymmetry of the flow area is the primary cause of the ebb dominance. Large waves can reduce the observed flow asymmetry owing to the relative reduction of ebb flows in the channel crossing the shoal.

Appendix A: Reynolds Stresses and Bottom Drag Coefficient

Two downward-facing ADVs were deployed 0.8 m above the seafloor in 2.5-m depth just offshore of the inlet mouth (Figure 1b, black square). The ADVs were separated 1.6 m horizontally and were sampled at 16 Hz from 2 to 22 May for 1,140 s (19 min) starting on the hour and 20 and 40 min past the hour. Horizontal velocities were rotated into local principal flow axes ($\theta_p = -65°$, Emery & Thomson, 2001).

Owing to the overlap in frequencies between wave orbital and turbulent motions, estimates of Reynolds stresses from measurements in shallow water are biased by surface gravity waves (Grant & Madsen, 1986; Trowbridge, 1998). The wave-induced bias was reduced by differencing the spatially separated measurements of horizontal and vertical velocity, assuming that the turbulent motions are not correlated with each other, and that the ADV separation is small relative to the wavelength of surface waves, but long relative to the correlation scale of turbulence (Trowbridge, 1998). Wave contamination also was evaluated by

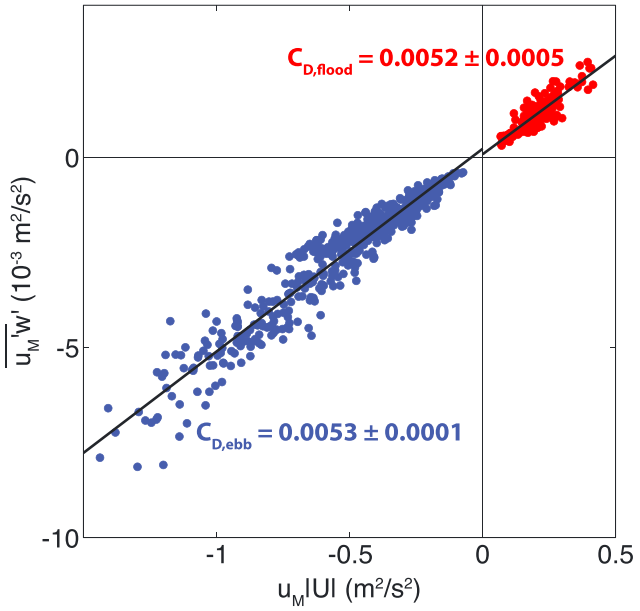

Figure A1. Reynolds stress estimates $\overline{u_M' w'}$ versus major axis velocity times mean speed ($u_M|U|$) for flood (red circles, slope [C_D] = 0.0052 ± 0.0005) and ebb (blue circles, slope [C_D] = 0.0053 ± 0.0001).

comparing the cospectra of the horizontal and vertical velocities with a semitheoretical model for one-dimensional turbulence (Gerbi et al., 2009; Kaimal et al., 1972; Trowbridge & Elgar, 2003):

$$\frac{Co_{uw}(k)}{\overline{u_M' w'}} = \left[1 - \frac{7}{3\pi}\sin\left(\frac{3\pi}{7}\right)\right]\frac{1/k_0}{1+\left(\frac{k}{k_0}\right)^{7/3}}, \quad \text{(A1)}$$

where $Co_{uw}(k)$ is the cospectrum between the major axis (u_M) and vertical velocities (w) as a function of wave number k=2π/λ, where λ is a turbulent length scale, $\overline{u'w'}$ is the covariance of the major axis and vertical velocity fluctuations, and k_0 is the rolloff wave number (the inverse length scale of the dominant flux-carrying eddies). The cospectral peak for the observed velocities was compared with that of the model for each burst.

Frequency-dependent cospectra were transformed to wave number spectra using the frozen turbulence hypothesis ($k = 2\pi f/U$, where f is the frequency, and U is the burst mean speed, Taylor, 1938). The frozen turbulence hypothesis breaks down in the presence of unsteady advection, owing to energetic waves or slow drift (Gerbi et al., 2009; Lumley & Terray, 1983). Thus, bursts with rms orbital velocities greater than the burst mean speed (22% of the data, mostly near slack) were discarded. Bursts with rms differences between normalized cospectra and the Kaimal model greater than 0.15 were discarded. The remaining bursts (46% of the measured time series) include times with local significant wave heights ranging from 0 to 0.7 m and currents ranging from −1.2 to 0.6 m/s.

Reynolds stresses ($\overline{u'w'}$) were estimated by integrating the cross-spectra of the horizontal and vertical velocities from 0.0312 to 8.000 Hz. To extrapolate the measured Reynolds stress estimates to near the seafloor, a linear stress profile $\tau_{b,\,\max} = \tau_{obs}H/(H-d)$ (where τ_{obs} is the measured Reynolds stress, H is the instantaneous depth, and d = 0.8 m is the measurement distance above the bottom) was assumed (i.e., the dominant balance is between a barotropic pressure gradient and vertical stress divergence; Geyer et al., 2000).

The near-bottom estimates of Reynolds stresses were compared with hourly averaged major axis velocity squared (the quadratic drag law for bottom stress, Figure A1) to estimate a bottom drag coefficient of C_D = 0.005, a value similar to previous studies at New River Inlet, NC (Chen et al., 2015; Wargula et al., 2014). Tidal and wave-driven changes to the bottom drag coefficient were negligible. However, 92% of bursts with local waves greater than 0.5 m were discarded in quality control, and thus the data may not resolve wave effects on the bottom stress.

Appendix B: The Importance of Advection to Resolving Flows and Wave Effects on the Mid-Shoal

The differences in modeled and observed flow responses to waves may be owing in part to the importance of the advection terms on the mid-shoal (Figure 1b, M). The dominant balance for the modeled momentum at the mid-shoal is between pressure gradient, local acceleration, total advection, and bottom stress (Figure A2b, r^2 = 1.00, slope = 0.99). Total advection, a momentum source or sink related to spatial gradients in the flows, plays a major role in model closure (compare best fit slopes in Figure A2a with those in Figure A2b). The wave forcing term is small (slopes of Figure A2b are close to 1) but is the primary cause of scatter in this simple momentum balance (normalized rms error > 10% in Figure A2b). The balance between pressure gradient, local acceleration, and bottom stress estimated with the direct model output (Figure A2a) is similar to the pointwise balance estimated from model output of velocities and water levels at instrument locations (Figure 5d), indicating that estimates of these terms are reasonably accurate. Thus, the lack of closure in the balance using the pointwise (or observed) cross-shore advection estimates may be owing to the poor spatial resolution of the cross-shore advection, as well as to the significance of alongshore advection. Further

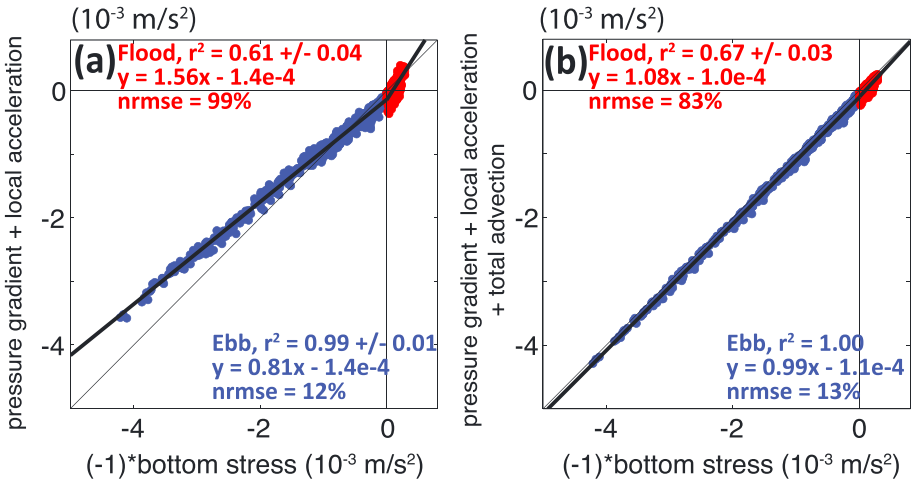

Figure A2. Depth-averaged, simulated (direct model output) cross-shore (a) pressure gradient and local acceleration and (b) pressure gradient, local acceleration, and total advection on the mid-shoal (Figure 1b, M) versus negative bottom stress for flood (red circles) and ebb (blue circles). The thin diagonal lines have a slope of 1, and the thick diagonal lines are the least squares fits (equations shown in the legends). The normalized (by bottom stress) root-mean-square errors (nrmses) are given for flood and ebb.

comparisons with observations at a finer spatial resolution are needed to resolve the importance of advection, as well as the wave effects on advection, in the momentum balance on an ebb shoal.

Acknowledgments

We thank the PVLAB field crew for their hard work, persistence, good humor, and efforts in less-than-pleasant conditions to collect this data set; Jesse McNinch and the staff of the U.S. Army Corps of Engineers Field Research Facility for providing bathymetry and assisting with instrument deployment; Jim Thomson for the onsite wind data; and the Coastal Ocean Research and Monitoring Program (Station 41038) for offshore wind data. We had many useful discussions with Jamie MacMahan, Tom Hsu, John Trowbridge, Malcolm Scully, and Rocky Geyer about subtidal pressure fluctuations, bottoms stresses, and bedforms at New River Inlet, and two anonymous reviewers provided suggestions that greatly improved the manuscript. The data used in this publication are available by contacting Britt Raubenheimer (britt@whoi.edu) or Steve Elgar (elgar@whoi.edu), or via https://pv-lab.org/ri-dri/. Funding was provided by the Office of Naval Research, the National Science Foundation, a National Defense Science and Engineering Graduate award, National Security Science and Engineering and Vannevar Bush Faculty Fellowships from the Office of the Assistant Secretary of Defense for Research and Engineering, and a WHOI Coastal Ocean Institute Student Research Award.

References

Apotsos, A., Raubenheimer, B., Elgar, S., & Guza, R. T. (2008). Wave-driven setup and alongshore flows observed onshore of a submarine canyon. *Journal of Geophysical Research*, *113*, C07025. https://doi.org/10.1029/2007JC004514

Apotsos, A., Raubenheimer, B., Elgar, S., Guza, R. T., & Smith, J. A. (2007). Effects of wave rollers and bottom stress on wave setup. *Journal of Geophysical Research*, *112*, C02003. https://doi.org/10.1029/2006JC003549

Battjes, J. A., & Janssen, J. P. (1978). Energy loss and set-up due to breaking of random waves. *Proceedings of the 16th International Coastal Engineering Conference* (pp. 570–587). ASCE, New York.

Bertin, X., Fortunato, A. B., & Oliveira, A. (2009). A modeling-based analysis of processes driving wave-dominated inlets. *Continental Shelf Research*, *29*(5-6), 819–834. https://doi.org/10.1016/j.csr.2008.12.019

Bertin, X., & Olabarrieta, M. (2016). Relevance of infragravity waves in a wave-dominated inlet. *Journal of Geophysical Research: Oceans*, *121*, 5418–5435. https://doi.org/10.1002/2015JC011444

Blanton, J. O., Lin, G., & Elston, S. A. (2002). Tidal current asymmetry in shallow estuaries and tidal creeks. *Continental Shelf Research*, *22*(11-13), 1731–1743. https://doi.org/10.1016/S0278-4343(02)00035-3

Booij, N., Ris, R. C., & Holthuijsen, L. H. (1999). A third-generation wave model for coastal regions: 1. Model description and validation. *Journal of Geophysical Research*, *104*(C4), 7649–7666. https://doi.org/10.1029/98JC02622

Boon, J. D., & Byrne, R. J. (1981). On basin hypsometry and the morphodynamic response of coastal inlet systems. *Marine Geology*, *40*(1-2), 27–48. https://doi.org/10.1016/0025-3227(81)90041-4

Buijsman, M. C., & Ridderinkhof, H. (2007). Long-term ferry-ADCP observations of tidal currents in the Marsdiep inlet. *Journal of Sea Research*, *57*(4), 237–256. https://doi.org/10.1016/j.seares.2006.11.004

Charnock, H. (1955). Wind stress on a water surface. *Quarterly Journal of the Royal Meteorological Society*, *81*(350), 639–640. https://doi.org/10.1002/qj.49708135027

Chen, C. -l. (1991). Unified theory on power laws for flow resistance. *Journal of Hydraulic Engineering*, *117*(3), 371–389. https://doi.org/10.1061/(ASCE)0733-9429(1991)117:3(371)

Chen, J. -L., Hsu, T. J., Shi, F., Raubenheimer, B., & Elgar, S. (2014). Hydrodynamic modeling of New River Inlet, North Carolina using NearCoM-TVD. *Coastal Engineering Proceedings*, *1*(34), 41. https://doi.org/10.9753/icce.v34.currents.41

Chen, J. -L., Hsu, T. -J., Shi, F., Raubenheimer, B., & Elgar, S. (2015). Hydrodynamic and sediment transport modeling of New River Inlet (NC) under the interaction of tides and waves. *Journal of Geophysical Research: Oceans*, *120*, 4028–4047. https://doi.org/10.1002/2014JC010425

Dodet, G., Bertin, X., Bruneau, N., Fortunato, A. B., Nahon, A., & Roland, A. (2013). Wave-current interactions in a wave-dominated tidal inlet. *Journal of Geophysical Research: Oceans*, *118*, 1587–1605. https://doi.org/10.1002/jgrc.20146

Elgar, S., Herbers, T. H. C., & Guza, R. T. (1994). Reflection of ocean surface gravity waves from a natural beach. *Journal of Physical Oceanography*, *24*(7), 1503–1511. https://doi.org/10.1175/1520-0485(1994)024<1503:ROOSGW>2.0.CO;2

Elgar, S., Raubenheimer, B., & Guza, R. T. (2001). Current meter performance in the surf zone. *Journal of Atmospheric and Oceanic Technology*, *18*(10), 1735–1746. https://doi.org/10.1175/1520-0426(2001)018<1735:CMPITS>2.0.CO;2

Elgar, S., Raubenheimer, B., & Guza, R. T. (2005). Quality control of acoustic Doppler velocimeter data in the surfzone. *Measurement Science and Technology*, *16*(10), 1889–1893. https://doi.org/10.1088/0957-0233/16/10/002

Emery, W. J., & Thomson, R. E. (2001). *Data analysis methods in physical oceanography* (2nd ed.). Amsterdam, Netherlands: Elsevier Science B. V.

Feddersen, F. (2004). Effect of wave directional spread on the radiation stress: Comparing theory and observations. *Coastal Engineering*, *51*(5-6), 473–481. https://doi.org/10.1016/j.coastaleng.2004.05.008

Feddersen, F., Olabarrieta, M., Guza, R. T., Winters, D., Raubenheimer, B., & Elgar, S. (2016). Observations and modeling of a tidal inlet dye tracer plume. *Journal of Geophysical Research: Oceans*, *121*, 7819–7844. https://doi.org/10.1002/2016JC011922

Friedrichs, C. T., & Aubrey, D. G. (1988). Non-linear tidal distortion in shallow well-mixed estuaries: A synthesis. *Estuarine, Coastal and Shelf Science*, *27*(5), 521–545. https://doi.org/10.1016/0272-7714(88)90082-0

Friedrichs, C. T., & Aubrey, D. G. (1994). Tidal propagation in strongly convergent channels. *Journal of Geophysical Research*, *99*(C2), 3321–3336. https://doi.org/10.1029/93JC03219

Gerbi, G. P., Trowbridge, J. H., Edson, J. B., Plueddemann, A. J., Terray, E. A., & Fredericks, J. J. (2009). Measurements of momentum and heat transfer across the air-sea interface. *Journal of Physical Oceanography*, *38*(5), 1054–1072. https://doi.org/10.1175/2007JPO3739.1

Geyer, W. R., Trowbridge, J. H., & Bowden, M. M. (2000). The dynamics of a partially mixed estuary. *Journal of Physical Oceanography*, *30*(8), 2035–2048. https://doi.org/10.1175/1520-0485(2000)030<2035:TDOAPM>2.0.CO;2

Gong, W., Chen, Y., Zhang, H., & Chen, Z. (2018). Effects of wave-current interaction on salt intrusion during a typhoon event in a highly stratified estuary. *Estuaries and Coasts*, *1-20*. https://doi.org/10.1007/s12237-018-0393-8

Grant, W. D., & Madsen, O. S. (1979). Combined wave and current interaction with a rough bottom. *Journal of Geophysical Research*, *84*(C4), 1797–1808. https://doi.org/10.1029/JC084iC04p01797

Grant, W. D., & Madsen, O. S. (1986). The continental-shelf bottom boundary layer. *Annual Review of Fluid Mechanics*, *18*(1), 265–305. https://doi.org/10.1146/annurev.fl.18.010186.001405

Hench, J. L., Blanton, B. O., & Luettich, R. A. (2002). Lateral dynamic analysis and classification of barotropic tidal inlets. *Continental Shelf Research*, *22*(18-19), 2615–2631. https://doi.org/10.1016/S0278-4343(02)00117-6

Hench, J. L., & Luettich, R. A. (2003). Transient tidal circulation and momentum balances at a shallow inlet. *Journal of Physical Oceanography*, *33*(4), 913–932. https://doi.org/10.1175/1520-0485(2003)33<913:TTCAMB>2.0.CO;2

Herbers, T. H. C., & Guza, R. T. (1990). Estimation of directional wave spectra from multi-component observations. *Journal of Physical Oceanography*, *20*(11), 1703–1724. https://doi.org/10.1175/1520-0485(1990)<1703:EODWSF>2.0.CO;2

Kaimal, J. C., Wyngaard, J. C., Izumi, Y., & Cote, O. R. (1972). Spectral characteristics of surface-layer turbulence. *Quarterly Journal of the Royal Meteorological Society*, *98*(417), 563–589. https://doi.org/10.1002/qj.49709841707

Kang, K., & Di Iorio, D. (2006). Depth- and current-induced effects on wave propagation into the Altamaha River Estuary, Georgia. *Estuarine Coastal and Shelf Science*, *66*(3–4), 395–408. https://doi.org/10.1016/j.ecss.2005.09.008

Kuik, A. J., van Vledder, G. P., & Holthuijsen, L. H. (1988). A method for the routine analysis of pitch-and-roll buoy wave data. *Journal of Physical Oceanography*, *18*(7), 1020–1034. https://doi.org/10.1175/1520-0485(1988)018<1020:AMFTRA>2.0.CO;2

Large, W., & Pond, S. (1981). Open ocean momentum flux measurements in moderate to strong winds. *Journal of Physical Oceanography*, *11*(3), 324–336. https://doi.org/10.1175/1520-0485(1981)011<0324:OOMFMI>2.0.CO;2

Lentz, S., Guza, R. T., Elgar, S., Feddersen, F., & Herbers, T. H. C. (1999). Momentum balances on the North Carolina inner shelf. *Journal of Geophysical Research*, *104*(C8), 18,205–18,226. https://doi.org/10.1029/1999JC900101

Li, C., & O'Donnell, J. (1997). Tidally driven residual circulation in shallow estuaries with lateral depth variation. *Journal of Geophysical Research*, *102*(C13), 27,915–27,929. https://doi.org/10.1029/97JC02330

Li, C., & O'Donnell, J. (2005). The effect of channel length on the residual circulation in tidally dominated channels. *Journal of Physical Oceanography*, *35*(10), 1826–1840. https://doi.org/10.1175/JPO2804.1

Longuet-Higgins, M. S., & Stewart, R. W. (1964). Radiation stresses in water waves; a physical discussion, with applications. *Deep-Sea Research*, *11*(4), 529–562. https://doi.org/10.1016/0011-7471(64)90001-4

Luettich, R. A., Westerink, J. J., & Scheffner, N. W. (1992). ADCIRC: An advanced three-dimensional model for shelves, coasts, and estuaries. Report 1. Theory and Methodology of ADCIRC 2DDI and ADCIRC 3-DL, *Dredging Research Program Technical Report* DRP-92-6, Coastal Engineering Research Center, U.S. Army Corps of Engineers, Waterways Experiment Station, p141.

Lumley, J. L., & Terray, E. A. (1983). Kinematics of turbulence convected by a random wave field. *Journal of Physical Oceanography*, *13*(11), 2000–2007. https://doi.org/10.1175/1520-0485(1983)013<2000:KOTCBA>2.0.CO;2

MacMahan, J., van de Kreeke, J., Reniers, A., Elgar, S., Raubenheimer, B., Thornton, E., et al. (2014). Fortnightly tides and subtidal motions in a choked inlet. *Estuarine, Coastal and Shelf Science*, *150*, 325–331. https://doi.org/10.1016/j.ecss.2014.03.025

Malhadas, M. S., Leitão, P. C., Silva, A., & Neves, R. (2009). Effect of coastal waves on sea level in Óbidos Lagoon, Portugal. *Continental Shelf Research*, *29*(9), 1240–1250. https://doi.org/10.1016/j.csr.2009.02.007

Nadaoka, K., & Kondoh, T. (1982). Laboratory measurements of velocity field structure in the surf zone by LDV. *Coastal Engineering Japan*, *25*(1), 125–145. https://doi.org/10.1080/05785634.1982.11924341

Olabarrieta, M., Geyer, W. R., & Kumar, N. (2014). The role of morphology and wave-current interaction at tidal inlets: An idealized modeling analysis. *Journal of Geophysical Research: Oceans*, *119*, 8818–8837. https://doi.org/10.1002/2014JC010191

Olabarrieta, M., Warner, J. C., & Kumar, N. (2011). Wave-current interaction in Willapa Bay. *Journal of Geophysical Research*, *116*, C12014. https://doi.org/10.1029/2011JC007387

Orescanin, M., Raubenheimer, B., & Elgar, S. (2014). Observations of wave effects on inlet circulation. *Continental Shelf Research*, *82*, 37–42. https://doi.org/10.1016/j.csr.2014.04.010

Pacheco, A., Ferreira, Ó., Williams, J. J., Garel, E., Vila-Concejo, A., & Dias, J. A. (2010). Hydrodynamics and equilibrium of a multiple-inlet system. *Marine Geology*, *274*(1-4), 32–42. https://doi.org/10.1016/j.margeo.2010.03.003

Piedracoba, S., Souto, C., Gilcoto, M., & Pardo, P. C. (2005). Hydrography and dynamics of the Ría de Ribadeo (NW Spain), a wave driven estuary. *Estuarine, Coastal and Shelf Science*, *65*(4), 726–738. https://doi.org/10.1016/j.ecss.2005.07.013

Putrevu, U., & Svendsen, I. A. (1999). Three-dimensional dispersion of momentum in wave-induced nearshore currents. *European Journal of Mechanics - B/Fluids*, *18*(3), 409–427. https://doi.org/10.1016/S0997-7546(99)80038-7

Raubenheimer, B., Elgar, S., & Guza, R. T. (1998). Estimating wave heights from pressure measured in sand bed. *Journal of Waterway, Port, Coastal, and Ocean Engineering*, *124*(3), 151–154. https://doi.org/10.1061/(ASCE)0733-950X(1998)124:3(151)

Raubenheimer, B., Guza, R. T., & Elgar, S. (2001). Field observations of wave-driven setdown and setup. *Journal of Geophysical Research*, *106*(C3), 4629–4638. https://doi.org/10.1029/2000JC000572

Ris, R. C., & Holthuijsen, L. H. (1996). Spectral modelling of current induced wave-blocking. In *Proceedings of 25th Conference on Coastal Engineering* (pp. 1246–1254). Orlando, FL.

Rogowski, P., Terrill, E., & Chen, J. (2014). Observations of the frontal region of a buoyant river plume using an autonomous underwater vehicle. *Journal of Geophysical Research: Oceans*, *119*, 7549–7567. https://doi.org/10.1002/2014JC010392

Salles, P., Voulgaris, G., & Aubrey, D. G. (2005). Contribution of nonlinear mechanisms in the persistence of multiple tidal inlet systems. *Estuarine, Coastal and Shelf Science*, *65*(3), 475–491. https://doi.org/10.1016/j.ecss.2005.06.018

Shi, F., Hanes, D. M., Kirby, J. T., Erikson, L., Barnard, P., & Eshleman, J. (2011). Pressure-gradient-driven nearshore circulation on a beach influenced by a large inlet-tidal shoal system. *Journal of Geophysical Research*, *116*, C04020. https://doi.org/10.1029/2010JC006788

Shi, F., Svendsen, I. A., Kirby, J. T., & Smith, J. M. (2003). A curvilinear version of a quasi-3D nearshore circulation model. *Coastal Engineering*, *49*(1–2), 99–124. https://doi.org/10.1016/S0378-3839(03)00049-8

Smagorinsky, J. (1963). General circulation experiments with the primitive equations. I. The basic experiment. *Monthly Weather Review*, *91*(3), 99–164. https://doi.org/10.1175/1520-0493(1963)091<0099:GCEWTP>2.3.CO;2

Smith, J. M. (2002). Wave pressure gauge analysis with current. *Journal of Waterway, Port, Coastal and Ocean Engineering*, *128*(6), 271–275. https://doi.org/10.1061/(ASCE)0733-950X(2002)128:6(271)

Soulsby, R. L., Hamm, L., Klopman, G., Myrhaug, D., Simons, R. R., & Thomas, G. P. (1993). Wave-current interaction within and outside the bottom boundary layer. *Coastal Engineering*, *21*(1–3), 41–69. https://doi.org/10.1016/0378-3839(93)90045-A

Speer, P. E., & Aubrey, D. G. (1985). A study of non-linear tidal propagation in shallow inlet/estuarine systems part II: Theory. *Estuarine, Coastal and Shelf Science*, *21*(2), 207–224. https://doi.org/10.1016/0272-7714(85)90097-6

Spydell, M. S., Feddersen, F., Olabarrieta, M., Chen, J., Guza, R. T., Raubenheimer, B., & Elgar, S. (2015). Observed and modeled drifters at a tidal inlet. *Journal of Geophysical Research: Oceans*, *120*, 4825–4844. https://doi.org/10.1002/2014JC010541

Stommel, H., & Farmer, H. G. (1952). *On the nature of estuarine circulation*, *Ref*. 52–88. Woods Hole, MA: Woods Hole Oceanographic Institution.

Svendsen, I. A. (1987). Analysis of surf zone turbulence. *Journal of Geophysical Research*, *92*(C5), 5115–5124. https://doi.org/10.1029/JC092iC05p05115

Svendsen, I. A., Haas, K., & Zhao Q. (2002). Quasi-3D nearshore circulation model SHORECIRC: Version 2.0, CACR-02-01 research report, Center for Applied Coastal Research, University of Delaware.

Taylor, G. I. (1938). The spectrum of turbulence. *Proceedings of the Royal Society of London*. *Series A, Mathematical and Physical Sciences*, *164*(919), 476–490. https://doi.org/10.1098/rspa.1938.0032

Trowbridge, J., & Elgar, S. (2003). Spatial scales of stress-carrying nearshore turbulence. *Journal of Physical Oceanography*, *33*(5), 1122–1128. https://doi.org/10.1175/1520-0485(2003)033<1122:SSOSNT>2.0.CO;2

Trowbridge, J. H. (1998). On a technique for measurement of turbulent shear stress in the presence of surface waves. *Journal of Atmospheric and Oceanic Technology*, *15*(1), 290–298. https://doi.org/10.1175/1520-0426(1998)015<0290:OATFMO>2.0.CO;2

Wargula, A., Raubenheimer, B., & Elgar, S. (2014). Wave-driven along-channel subtidal flows in a well-mixed ocean inlet. *Journal of Geophysical Research: Oceans*, *119*, 2987–3001. https://doi.org/10.1002/2014JC009839

Zippel, S., & Thomson, J. (2015). Wave breaking and turbulence at a tidal inlet. *Journal of Geophysical Research: Oceans*, *120*, 1016–1031. https://doi.org/10.1002/2014JC010025